

Green Pea Galaxies and cohorts: Luminous Compact Emission-Line Galaxies in the Sloan Digital Sky Survey

Yuri I. Izotov

Main Astronomical Observatory, Ukrainian National Academy of Sciences, 27 Zabolotnoho str., Kyiv 03680, Ukraine

izotov@mao.kiev.ua

Natalia G. Guseva

Main Astronomical Observatory, Ukrainian National Academy of Sciences, 27 Zabolotnoho str., Kyiv 03680, Ukraine

guseva@mao.kiev.ua

and

Trinh X. Thuan

Astronomy Department, University of Virginia, P.O. Box 400325, Charlottesville, VA 22904-4325

txt@virginia.edu

ABSTRACT

We present a large sample of 803 star-forming luminous compact galaxies (LCGs) in the redshift range $z = 0.02 - 0.63$, selected from Data Release 7 of the Sloan Digital Sky Survey (SDSS). The global properties of these galaxies are similar to those of the so-called “green pea” star-forming galaxies, in the redshift range $z = 0.112 - 0.360$ and selected from the SDSS on the basis of their green color and compact structure. In contrast to green pea galaxies, our LCGs are selected on the basis of both their spectroscopic and photometric properties, resulting in a ~ 10 times larger sample, with galaxies spanning a redshift range $\gtrsim 2$ times larger. We find that the oxygen abundances and the heavy element abundance ratios in LCGs do not differ from those of nearby low-metallicity blue compact dwarf (BCD) galaxies. The median stellar mass of LCGs is $\sim 10^9 M_\odot$. However, for galaxies with high $\text{EW}(\text{H}\beta)$, $\geq 100\text{\AA}$, it is only $\sim 7 \times 10^8 M_\odot$. The star formation rate in LCGs varies in the large range of $0.7 - 60 M_\odot \text{ yr}^{-1}$, with

a median value of $\sim 4 M_{\odot} \text{ yr}^{-1}$, a factor of ~ 3 lower than in high-redshift star-forming galaxies at $z \gtrsim 3$. The specific star formation rates in LCGs are extremely high and vary in the range $\sim 10^{-9} - 10^{-7} \text{ yr}^{-1}$, comparable to those derived in high-redshift galaxies.

Subject headings: galaxies: abundances — galaxies: irregular — galaxies: ISM
— galaxies: star formation — H II regions

1. Introduction

Recently, Cardamone et al. (2009) reported on a new class of luminous compact galaxies at redshifts $z = 0.112 - 0.360$, discovered by the Galaxy Zoo project from the Sloan Digital Sky Survey (SDSS) images. The Galaxy Zoo project collected simple morphological classifications of nearly 900 000 galaxies drawn from the SDSS, contributed by hundreds of thousands of volunteers (Lintott et al. 2008, 2011). In particular, the attention was drawn on compact objects named “green pea” galaxies. Their appearance is mainly caused by the very strong [O III] $\lambda 5007\text{\AA}$ optical emission line, with an unusually large equivalent width of up to $\sim 1000 \text{\AA}$, redshifting into the SDSS r band, resulting in a green color in the *gri* composite SDSS images (green being the color represented by the r band in these composite images). Cardamone et al. (2009) discussed a well-defined sample of 251 color-selected objects located mainly in low-density regions. They found that the median environmental density around the green pea galaxies is less than two-thirds of that around normal galaxies. Most of the green pea galaxies are strongly star-forming, although there are some active galactic nuclei interlopers, including eight newly discovered narrow-line Seyfert 1 galaxies. For a further spectroscopic analysis, Cardamone et al. (2009) selected a subsample of 80 star-forming galaxies and found that they are low-mass galaxies ($M \sim 10^{8.5} - 10^{10} M_{\odot}$), with high star formation rates ($\sim 10 M_{\odot} \text{ yr}^{-1}$) and solar metallicities, if the solar calibration of Asplund et al. (2009), $12 + \log (\text{O}/\text{H})_{\odot} = 8.7$, is adopted. Cardamone et al. (2009) found that green pea galaxies have some of the highest specific star formation rates seen in the local Universe (up to $10^{-8} M_{\odot} \text{ yr}^{-1}$), and are similar in size, mass, luminosity and metallicity to luminous blue compact galaxies. They are also similar to high-redshift ultraviolet-luminous galaxies (Lyman-break galaxies and Ly- α emitters). Those authors suggested that the green pea galaxies may be the last remnants of a mode of star formation common in the early Universe, and therefore provide an excellent local laboratory for studying the extreme star formation processes that occur in high-redshift galaxies.

Later, Amorín et al. (2010) investigated the oxygen and nitrogen chemical abundances in the green pea galaxies of Cardamone et al. (2009). They found these systems to be

genuine metal-poor galaxies, with mean oxygen abundances $12 + \log \text{O}/\text{H} \sim 8.0$, or 0.2 solar. While the N/O ratios of green pea galaxies follow the relation with stellar mass of local star-forming galaxies, Amorín et al. (2010) find that the green pea mass-metallicity relation is offset by ~ 0.3 dex to lower metallicities. They argue that recent interaction-induced inflow of gas, possibly coupled with a selective metal-rich gas loss, driven by supernova winds, may explain their findings. Interaction-induced infall of gas would also be consistent with the known galaxy properties such as high specific star formation rates, extreme compactness, and disturbed optical morphologies. Amorín et al. (2010) concluded that the green pea galaxy properties seem to be not common in the nearby universe, suggesting that the green pea phase is a short and extreme stage of their evolution. They agreed with Cardamone et al. (2009) that these galaxies may allow to study in great detail many processes, such as starburst activity and chemical enrichment, under physical conditions approaching those in galaxies at higher redshifts.

In this paper, we wish to further the studies of green pea galaxies and reexamine the above conclusions of Cardamone et al. (2009) and Amorín et al. (2010) by studying a considerably larger sample of luminous compact emission-line galaxies selected from the Data Release 7 (DR7) of the Sloan Digital Sky Survey (Abazajian et al. 2009). We adopt an entirely different approach in the selection of our galaxy sample. In contrast to the study of Cardamone et al. (2009), our luminous compact galaxies are selected using spectroscopic criteria which are supplemented by morphological criteria. The selection criteria of our galaxies are described in Section 2. Their element abundances are derived in Section 3. The luminosity-metallicity relation for the sample galaxies is discussed in Section 4. In Section 5 we describe a technique for galaxy stellar mass determination, taking into account the gaseous continuum emission. We derive stellar masses for the young and old stellar populations in each galaxy. In Section 6 we compare the physical properties of starbursts in luminous compact galaxies. The mass-metallicity relation for the sample galaxies is derived in Section 7. In Sections 8 and 9, we examine respectively their star formation rates and the age of their stellar populations. Our conclusions are presented in Section 10.

2. A sample of luminous compact galaxies

2.1. Selection criteria

The photometric selection criteria used by Cardamone et al. (2009), based on the green appearance of a galaxy in the SDSS images, pick out galaxies in a relatively narrow range of redshifts, $z \sim 0.1 - 0.3$: those redshifts are such as to make the strong $\text{H}\beta$, $[\text{O III}] \lambda 4959\text{\AA}$ and $[\text{O III}] \lambda 5007\text{\AA}$ optical emission lines fall in the SDSS r band. Such an approach fails to

find galaxies with similar properties at lower and higher redshifts because their colors would then not be green.

To avoid this restriction, we adopt here a different approach. We select luminous compact emission-line galaxies (LCGs) by using criteria that are based on both spectra and images in the SDSS DR7. These criteria are as follows:

1) the extinction-corrected luminosity of the $H\beta$ emission line is greater than $L(H\beta) = 3 \times 10^{40} \text{ erg s}^{-1}$. The extinction coefficient is derived from the observed Balmer decrement in the SDSS spectra.

2) the equivalent width of the $H\beta$ emission line is high, $EW(H\beta) \gtrsim 50 \text{ \AA}$. This criterion helps to select only objects with strong emission lines in their spectra (Fig. 1), and thus containing young starbursts with ages 3 - 5 Myr. We note that most of the green pea galaxies from Cardamone et al. (2009) have $EW(H\beta) \gtrsim 100 \text{ \AA}$. Thus, our sample of LCGs covers a larger range of $EW(H\beta)$.

Contrary to Cardamone et al. (2009), we do not use the equivalent width of the [O III] $\lambda 5007$ emission line as a selection criterion. This is because the strength of the [O III] $\lambda 5007$ emission line in young starbursts is metallicity-dependent. It is strongest at $12 + \log O/H \sim 8.0$, decreasing at both higher and lower O abundances. Therefore, using the strength the [O III] $\lambda 5007$ emission line as a selection criterion would unduly bias the sample toward galaxies with a narrow range of O abundances near $12 + \log O/H \sim 8.0$. On the other hand, the use of the $H\beta$ emission line allows us to pick out galaxies with a considerably larger range of O abundances.

3) only galaxies with a well-detected [O III] $\lambda 4363 \text{ \AA}$ emission line in their spectra, with a flux error less than 50% of the line flux, are selected. This criterion allows an accurate abundance determination using the direct method, in contrast to Cardamone et al. (2009) who used the less accurate empirical strong-line method for abundance determination. If we do not impose criterion 3, but only criteria 1 and 2, then the number of selected galaxies would increase only by $\sim 20\%$. Thus, when criterion 3 is imposed, the decrease in the number of galaxies is small enough so as not to introduce large biases in the physical properties of the selected sample. On the other hand, the benefit of being able to determine accurate O abundances and study trends with metallicity is inestimable.

4) galaxies with obvious evidence of Seyfert 2 spectral features, such as strong [Ne V] $\lambda 3426$, He II $\lambda 4686$, [O I] $\lambda 6300$, and [S II] $\lambda 6717$, $\lambda 6731$ emission lines are excluded. Thus, we select only star-forming galaxies.

5) on their SDSS images, galaxies are nearly compact at low redshifts, and unresolved

at high redshifts.

Using these criteria, we constructed 4 subsamples of LCGs: 1) subsample 1 includes 161 galaxies with $\text{EW}(\text{H}\beta) \geq 100\text{\AA}$ and a round shape, without evident signs of disturbed morphology. Thus, this subsample should be most similar in properties to the star-forming green pea galaxy sample of Cardamone et al. (2009); 2) subsample 2 consists of 159 galaxies with $\text{EW}(\text{H}\beta) \geq 100\text{\AA}$ and with some sign of disturbed morphology suggesting interaction and the presence of more than one star-forming region; 3) subsample 3 is the same as subsample 1, but it consists of 116 galaxies with a lower $\text{EW}(\text{H}\beta)$, covering the range $100\text{\AA} > \text{EW}(\text{H}\beta) \geq 50\text{\AA}$; and 4) subsample 4 is the same as subsample 2, but it consists of 367 galaxies with a lower $\text{EW}(\text{H}\beta)$, $100\text{\AA} > \text{EW}(\text{H}\beta) \geq 50\text{\AA}$. The galaxies from subsample 4 often show two or more compact knots of star formation. Thus, the total number of selected galaxies is 803, or ~ 10 times larger than the sample of star-forming green pea galaxies of Cardamone et al. (2009). In general, the selected LCGs are faint objects with low extinction. Their median SDSS g apparent magnitude and reddening $E(B - V)$ range from 20.3 and 0.10 for subsample 1 to 18.4 and 0.15 for subsample 4 (Table 1).

2.2. A Luminosity Upper Limit

The distribution of the $\text{H}\beta$ luminosity $L(\text{H}\beta)$ with redshift z is shown in Fig. 2. It is seen that the selected galaxies span a large range of redshifts, from ~ 0.02 to ~ 0.63 . The apparent increase of $L(\text{H}\beta)$ with redshift, for $z \lesssim 0.2$, is likely the result of a selection effect (called the Malmquist bias): only the brightest galaxies at high redshift were observed spectroscopically in the SDSS. Fig. 2 shows that galaxies with $\text{EW}(\text{H}\beta) \geq 100\text{\AA}$ are distributed more uniformly with redshift than those with lower $\text{EW}(\text{H}\beta)$, which tend to populate the lower redshift region. This difference is likely also due to a selection effect. The $[\text{O III}] \lambda 4363\text{\AA}$ emission line in objects with a high $\text{EW}(\text{H}\beta)$ is stronger. Hence it can be measured with a good accuracy even in high redshift objects, which helps to fulfill the selection criterion 3 above and allows the inclusion of the galaxy in the LCG sample.

Fig. 2 shows a remarkable feature: there is an upper limit of $L(\text{H}\beta)$ at the level of $\sim 2.5 \times 10^{42} \text{ erg s}^{-1}$ (shown by the horizontal dashed line), which is almost not redshift dependent, despite the fact that none of our selection criteria sets an upper limit to the $\text{H}\beta$ luminosity. The presence of this upper limit suggests the existence of a self-regulating mechanism in star formation which somehow forbids the formation of more luminous star-forming regions. There is probably a negative feedback mechanism due to the intense UV radiation of the present starburst which prevents further star formation in LCGs. While beyond the scope of the present paper, the role of the ionizing radiation from young massive

starbursts in shutting off star formation beyond a given threshold luminosity, should be investigated.

2.3. Blue compact dwarf, green pea and luminous compact galaxies: a continuum in luminosity

The range of z in Fig. 2 is ~ 2.5 times larger than that for the green pea galaxies of Cardamone et al. (2009). Those authors and Amorín et al. (2010) suggested that green pea galaxies form a new class of objects. We will argue now that this is not the case and that they are just a subset of LCGs. Nearby ($z \sim 0$) luminous compact emission-line galaxies have been known for decades. Examples of such objects are, in order of decreasing $L(\text{H}\beta)$ (we give the logarithm of the aperture- and extinction-corrected $L(\text{H}\beta)$ in parentheses for each object in units of erg s^{-1}): Mrk 930 (41.57), SBS 0335–052E (41.24), HS 0837+4717 (41.10) and II Zw 40 (40.81). Some of them have been studied in great detail (see e.g. the studies of SBS 0335–052E by Izotov et al. 1990, 1997; Thuan et al. 1997; Thuan & Izotov 2005). These objects are known as blue compact dwarf galaxies (BCD) and are plotted as large open circles in Fig. 2. A recent review of BCD properties is given by Thuan (2008). We see that the $L(\text{H}\beta)$ of these BCDs are comparable to those of LCGs at the low-luminosity end of the sample. Other well-known BCDs have lower $L(\text{H}\beta)$, below our cut-off: Tol1214–277 (40.43), I Zw 18 (39.72 for a distance of 15 Mpc) and Mrk 209 (39.55). In other words, LCGs are the same type of objects as BCDs except that they are more luminous in the mean.

By the same token, green pea galaxies do not form a distinct class of objects from LCGs. They are just a subsample of the class of LCGs, in a restricted redshift range. At other redshifts, the same galaxies would not look green, but blue, pink or brown. This is illustrated in Fig. 3 where we show SDSS images of eight galaxies from our LCG sample, located at different distances. LCGs in the upper panel are galaxies from subsample 1 with round shape, while those in the lower panel are galaxies from subsample 2 with extended emission and/or disturbed morphology. It is seen that, as the strong emission lines (the Balmer lines and the [O III] $\lambda 4959\text{\AA}$, $\lambda 5007\text{\AA}$ lines) shift through the different SDSS filters, the colors of the LCGs as seen in the composite SDSS *gri* images change with redshift. They are blue at low redshifts, becoming pink at $z \lesssim 0.1$, green at $z \sim 0.2$ and brown at $z \sim 0.6$.

We next compare the colors of the LCGs to those of normal galaxies and QSOs. We show in Fig. 4 the $g - r$ vs $r - i$ color-color diagram for LCGs (filled and open circles and triangles). For comparison are also shown representative objects classified in the SDSS as galaxies (black dots) and QSOs (Schneider et al. 2010) (grey dots). The $g - r$ and $r - i$ colors for LCGs span very large ranges, extending over 2.5 mag and 3.5 mag respectively. These

ranges are the largest for LCGs with a high $H\beta$ equivalent width $EW(H\beta) \gtrsim 100\text{\AA}$ (filled symbols). Such large color ranges are not due to differences in galaxy physical properties, but to a large redshift range. Galaxies with strong emission lines at $z \sim 0.1 - 0.3$ would appear in the left upper corner of the diagram, while the same galaxies at $z \sim 0.4 - 0.5$ would occupy the region with $r - i > 1.0$, in the extreme right part of the diagram. The location of the LCGs in the $g - r$ vs $r - i$ diagram is very different from that of the bulk of galaxies without or with weak line emission in their spectra (grey dots). It is interesting to note that many LCGs are located in the region with $(g - r, r - i) \sim (0.0 - 0.5, 0.0 - 0.5)$ populated by QSOs. A significant fraction of these LCGs are automatically classified in the SDSS as QSOs because of their compact morphology, while their spectra are that of star-forming galaxies rather than AGNs.

What is the overlap between the green pea sample of Cardamone et al. (2009) and our LCG sample? Cardamone et al. (2009) selected star-forming green pea galaxies by requiring them to be in the left upper region of the $(g - r, r - i)$ diagram, delineated by the two straight lines in Fig. 4. We have encircled in this figure all the 66 LCGs that are also in the green pea sample of Cardamone et al. (2009). The latter sample contains a total of 80 objects. Out of the 14 missing objects, 12 were rejected because of their noisy spectra with a non-detected or weak $[O\text{ III}] \lambda 4363$ emission line, although they were present in the initial sample. Thus, our LCG selection criteria missed only two green pea star-forming galaxies out of a total of 80 galaxies, i.e. the overlap factor between the green pea and LCG samples is 98%! On the other hand, more than half of the LCGs in the region of green pea star-forming galaxies delineated by the two straight lines were not selected by Cardamone et al. (2009). All these galaxies have a green color on the SDSS images and are at redshifts $z \sim 0.1 - 0.3$. As for the remaining LCGs, to the right of the solid lines in the color-color diagram, they have redshifts $z < 0.1$ or $z > 0.3$, and would not be picked up by the green pea selection criteria, although they are the same type of objects, but at different redshifts.

2.4. Low-metallicity AGNs in Green Pea Galaxies

It is interesting to note that the $H\beta$ luminosities of the five known low-metallicity compact galaxies that are thought to contain AGNs, as evidenced by the strong broad components of their $H\alpha$ and $H\beta$ emission lines (Izotov & Thuan 2008; Izotov et al. 2010) put them in the class of LCGs. These objects fulfill all the selection criteria discussed above for LCGs. They are shown by the large filled circles in Fig. 2. Their redshifts are in the range 0.1–0.3, and therefore they can also be classified as green pea galaxies. However, in the $(g - r) - (r - i)$ color-color diagram in Fig. 4, only two low-metallicity AGNs fall into the

green pea region. The two other low-metallicity AGNs are located outside both the green pea and LCG regions. The latter two objects show abnormally red $g - r$ and $r - i$ colors, probably due to high dust extinction. The fifth low-metallicity AGN studied by Izotov et al. (2010) is not shown in Fig. 4 because it is beyond the SDSS sky area and therefore we have no g, r, i colors for it.

It is not unreasonable that AGNs tend to occur in more luminous and hence more massive compact galaxies, as these have more massive star formation and hence are more favorable to the formation of intermediate-mass black holes. It would be interesting to obtain high-resolution and high signal-to-noise ratio spectra of more objects in the LCG sample to look for more objects with broad components which may contain AGNs.

2.5. The $[\text{O III}] \lambda 5007/\text{H}\beta$ vs. $[\text{N II}] \lambda 6583/\text{H}\alpha$ diagram

Figure 5 shows by small filled and open symbols the positions of LCGs in the $[\text{O III}] \lambda 5007/\text{H}\beta$ vs. $[\text{N II}] \lambda 6583/\text{H}\alpha$ diagram (Baldwin et al. 1981, hereafter BPT). The star and filled square represent respectively the well-studied BCDs SBS 0335–052E and HS 0837+4717. HS 0837+4717 lies in the same region as the LCGs while SBS 0335–052E lies to the left, having an abnormally low $[\text{N II}] \lambda 6583/\text{H}\alpha$ ratio. This is because SBS 0335–052E has a low N/O abundance ratio, a characteristic of extremely low-metallicity BCDs (e.g. Izotov et al. 2006), and the ionizing parameter of its H II region is high, resulting in a small abundance of singly ionized nitrogen. For comparison, the grey dots represent all galaxies from the SDSS DR7 with flux errors smaller than 10% for each of the four emission lines $\text{H}\beta$, $[\text{O III}] \lambda 5007$, $\text{H}\alpha$ and $[\text{N II}] \lambda 6583$. The emission line fluxes for the SDSS galaxies shown by grey dots were measured using the technique developed by Tremonti et al. (2004) and are taken from the SDSS website ¹. These galaxies are distributed into two wings, the left one thought to contain star-forming galaxies and the right one AGN hosts. The dashed line represents the empirical divisory line between star-forming galaxies and AGNs proposed by Kauffmann et al. (2003), while the continuous line represents the upper limit for pure star-forming galaxies taken from Stasińska et al. (2006). We see that the LCGs lie in the low-metallicity part of what is usually considered as the region of star-forming galaxies. We note that the five low-metallicity AGN candidates from Izotov & Thuan (2008) and Izotov et al. (2010), represented by large filled circles, lie in the same region as the LCGs. The BPT diagram cannot distinguish between star-forming galaxies and AGN hosts in the low-metallicity regime.

¹http://www.sdss.org/DR7/products/value_added/index.html.

3. Element abundances

We derived element abundances in all 803 LCGs from the narrow emission-line fluxes, using the so-called direct method. This method is based on the determination of the electron temperature within the [O III] zone from the [O III] λ 4363/ $(\lambda$ 4959+ λ 5007) line ratio. The fluxes in all spectra were measured using Gaussian fitting with the IRAF² SPLOT routine. They were corrected for both extinction, using the reddening curve of Whitford (1958), and underlying hydrogen stellar absorption, derived simultaneously by an iterative procedure described by Izotov et al. (1994) and using the observed decrements of the narrow hydrogen Balmer lines. The extinction coefficient $C(\text{H}\beta)$ and equivalent width of hydrogen absorption lines $\text{EW}(\text{abs})$ are derived in such a way to obtain the closest agreement between the extinction-corrected and theoretical recombination hydrogen emission-line fluxes normalized to the $\text{H}\beta$ flux. It is assumed that $\text{EW}(\text{abs})$ is the same for all hydrogen lines. This assumption is justified by the evolutionary stellar population synthesis models of González Delgado et al. (2005).

The physical conditions, and the ionic and total heavy element abundances in the H II regions were derived following Izotov et al. (2006). In particular for O^{2+} , Ne^{2+} , and Ar^{3+} abundances, we adopt the temperature $T_e(\text{O III})$ directly derived from the [O III] λ 4363/ $(\lambda$ 4959 + λ 5007) emission-line ratio. The electron temperatures $T_e(\text{O II})$ and $T_e(\text{S III})$ were derived from the empirical relations by Izotov et al. (2006). We used $T_e(\text{O II})$ for the calculation of O^+ , N^+ , S^+ , and Fe^{2+} abundances and $T_e(\text{S III})$ for the calculation of S^{2+} , Cl^{2+} , and Ar^{2+} abundances. The electron number densities $N_e(\text{S II})$ were obtained from the [S II] λ 6717/ λ 6731 emission-line ratios, respectively. The low-density limit holds for the H II regions that exhibit the emission lines considered here. The element abundances then do not depend sensitively on N_e . We use the ionization correction factors (ICFs) from Izotov et al. (2006) to correct for unseen stages of ionization and to derive the total O, N, Ne, S, Cl, Ar, and Fe abundances.

The dependence of the oxygen abundance $12 + \log \text{O}/\text{H}$ of the LCGs on their redshift z is shown in Fig. 6a. There is no clear variation of $12 + \log \text{O}/\text{H}$ with z . The median value of $12 + \log \text{O}/\text{H}$ for the whole sample is ~ 8.11 or 0.26 solar (Table 1). This median value is similar to the one obtained by Amorín et al. (2010) for the subsample of the green pea galaxies of Cardamone et al. (2009) they used. However, our values of $12 + \log \text{O}/\text{H}$ are significantly lower – by ~ 0.6 dex – than those obtained by Cardamone et al. (2009). This

²IRAF is the Image Reduction and Analysis Facility distributed by the National Optical Astronomy Observatory, which is operated by the Association of Universities for Research in Astronomy (AURA) under cooperative agreement with the National Science Foundation (NSF).

difference is due to the different techniques used to derive abundances. We have used the direct method while Cardamone et al. (2009) have used an empirical calibration method based on the $[\text{N II}] \lambda 6583/\text{H}\alpha$ flux ratio, despite the fact that nearly all their spectra contain a strong enough $[\text{O III}] \lambda 4363$ emission line, which can be used to determine the electron temperature of the $[\text{O III}]$ zone. Evidently, there is an offset between oxygen abundances derived by the direct method and those derived by the strong-line empirical method used by Cardamone et al. (2009). A more detailed comparison between abundances obtained by us and by Cardamone et al. (2009) is given in Section 5.3.

Fig. 6a also shows that LCGs with lower equivalent widths $\text{EW}(\text{H}\beta)$ (open symbols) have systematically higher $12 + \log \text{O}/\text{H}$ than LCGs with higher equivalent widths (filled symbols). While the median $12 + \log \text{O}/\text{H}$ is 8.04 for subsample 1, it is 8.16 for subsample 4 (Table 1). This effect is more pronounced in Fig. 6b where we show the dependence of $12 + \log \text{O}/\text{H}$ on $\text{EW}(\text{H}\beta)$. The LCGs with high $\text{EW}(\text{H}\beta) > 200\text{\AA}$ are more metal-poor than LCGs with lower $\text{EW}(\text{H}\beta)$ by ~ 0.2 dex. Such variations can be explained by the fact that LCGs with a lower $\text{EW}(\text{H}\beta)$ are in general more massive and thus more metal-rich (see the discussion of the mass-metallicity relation below).

In Fig. 7, we show the dependence of the N/O , Ne/O , S/O , Cl/O , Ar/O and Fe/O abundance ratios on the oxygen abundance $12 + \log \text{O}/\text{H}$ for the LCG sample (filled circles). For comparison, we also show a sample of BCDs that has been collected primarily to study helium abundances in low-metallicity dwarf galaxies. This sample is the same as in Izotov et al. (1994), with the addition of galaxies from Izotov & Thuan (2004) and includes mainly nearby low-metallicity and low-luminosity galaxies. It is seen from Fig. 7 that the distribution of heavy element abundance ratios in LCGs is very similar to those in BCD galaxies, despite the fact that LCGs have higher oxygen abundances ($12 + \log \text{O}/\text{H} \gtrsim 7.6$), while the BCD galaxies span a larger range of metallicities, with $12 + \log \text{O}/\text{H}$ as low as 7.12. This implies that the chemical enrichment history has been very similar in BCDs and LCGs.

The N/O vs O/H diagram (Fig. 7a) shows a significant spread of N/O values, in the range -0.9 - -1.7 at $12 + \log \text{O}/\text{H} \gtrsim 7.6$, for both the LCG and BCD samples. However, there is no appreciable increase of N/O with increasing $12 + \log \text{O}/\text{H}$ up to ~ 8.4 , suggesting that nitrogen is mainly of primary origin in LCGs. This is at variance with the results of Amorín et al. (2010) who find a clear increase of N/O with $12 + \log \text{O}/\text{H}$ over the whole 7.5 - 8.4 range, suggesting that secondary production of nitrogen is important. Additionally, Amorín et al. (2010) derived a high $\log \text{N}/\text{O}$, larger than the solar ratio of -0.86 (Asplund et al. 2009), in a significant number of green pea galaxies with $12 + \log \text{O}/\text{H}$ in the range ~ 8.1 - 8.4. The reason for the differences between our results and those

of Amorín et al. (2010) is not clear. We note that Amorín et al. (2010) used the pipeline measurements of line fluxes available in the SDSS archive, while we measured them directly using the SDSS spectra, taking into account the possible contamination of [N II] $\lambda 6583$ by H α $\lambda 6563$.

It is worth noting the increase of the Ne/O abundance ratio and the decrease of the Fe/O ratio with increasing oxygen abundance. These trends are caused by the depletion of O and Fe onto dust grains, as discussed by Izotov et al. (2006). The LCG data confirm these trends.

4. Luminosity-metallicity relation

The relation between the oxygen abundance $12 + \log \text{O}/\text{H}$ and the extinction-corrected absolute magnitude M_g in the SDSS g band for LCGs is shown in Fig. 8. The symbols for LCGs are the same as in Fig. 2. The g apparent magnitudes are taken from the SDSS data base. The correction for extinction is done using the extinction coefficient $C(\text{H}\beta)$ obtained from the hydrogen Balmer decrement in the SDSS optical spectra. Distances of LCGs are derived from redshifts and adopting a Hubble constant $H_0 = 75 \text{ km s}^{-1} \text{ Mpc}^{-1}$. For comparison, we show by dots the emission-line galaxy sample of Guseva et al. (2009). We also show by large filled circles the three most metal-deficient BCDs known in the local universe, I Zw 18, SBS 0335–052W and SBS 0335–052E (Guseva et al. 2009). The intermediate-redshift ($z < 1$) extremely low-metallicity emission-line galaxies studied by Kakazu et al. (2007) are shown by large filled squares, while the luminous metal-poor star-forming galaxies at $z \sim 0.7$ studied by Hoyos et al. (2005) are shown by large filled triangles. The dotted-line rectangle indicates the location of the Lyman-break galaxies (LBG) at $z \sim 3$ of Pettini et al. (2001). The solid line is the luminosity-metallicity relation derived by Guseva et al. (2009) for their emission-line galaxy sample (solid line in their Fig. 9).

LCGs are clearly offset by ~ 2 mag to brighter magnitudes as compared to the bulk of the local emission-line galaxies, implying strong ongoing star formation. There exists a similar offset for the three most-metal deficient BCDs I Zw 18, SBS 0335–052W and SBS 0335–052E, the intermediate-redshift extremely metal-poor emission-line galaxies of Kakazu et al. (2007), the luminous metal-poor emission-line galaxies at $z \sim 0.7$ of Hoyos et al. (2005) and the LBGs of Pettini et al. (2001). It appears that all these types of galaxies are undergoing strong bursts of star formation and that they define a common luminosity-metallicity relation, the one for actively star-forming galaxies, going from the most-metal deficient BCDs at the faint end to LBGs at the bright end. The best linear likelihood fit to the strongly star-forming galaxies, excluding LBGs for which the oxygen abundances are derived by using

not the direct but the strong-line method, is

$$12 + \log \text{O}/\text{H} = (-0.16 \pm 0.01) \times M_g + (4.86 \pm 0.19). \quad (1)$$

It is shown by a dashed line in Fig. 8.

Our LCGs, despite their lower redshift range ($z \sim 0.02 - 0.63$), are very similar in luminosity to the luminous galaxies at $z \sim 0.7$ of Hoyos et al. (2005), but they are, in the mean, some 3 mag fainter than LBGs. However, the most luminous objects in our LCG sample do have oxygen abundances and luminosities that are similar to those of LBGs at $z \sim 3$, implying that these two types of objects are likely of the same nature. In particular, most of the LCGs inside the LBG dotted rectangle (Fig. 8) have disturbed morphologies and relatively low equivalent widths $\text{EW}(\text{H}\beta)$. This implies some kind of gravitational interactions and/or merging processes in the galaxies with the significant fraction of a non-ionizing stellar population that contributes non-negligibly to the observed stellar continuum. The similarity in properties between LCGs and LBGs suggests that, since LCGs are relatively nearby, the bulk of them being in the redshift range $0 - 0.3$, they can be studied in detail to shed light on the physical properties of distant LBGs with $z \sim 3$.

5. Stellar masses

The stellar mass of a galaxy is one of its most important global characteristics. It can be derived by modeling its spectral energy distribution (SED) which depends on the adopted star formation history. However, in the case of LCGs, the situation is complicated by the presence of strong ionized gas emission, which must be subtracted before stellar mass determination. Cardamone et al. (2009) did consider the effect of the strong nebular emission lines. However, they did not take into account the effect of the gaseous continuum emission which is significant in spectra of LCGs with a high $\text{EW}(\text{H}\beta)$. Neglecting the correction for gaseous continuum emission would result in a significant overestimate of the galaxy stellar mass for two reasons: 1) gaseous continuum emission increases the luminosity of the galaxy; and 2) the SED of gaseous continuum emission is flatter than that of stars, making the SED redder than expected for pure stellar emission. Consequently, the fraction of the light from the red old stellar population is artificially increased. Therefore, to derive the correct stellar mass of the galaxy, we have used the method described below that takes into account the contribution of gaseous continuum emission.

5.1. Method

The method consists of fitting a series of model SEDs to the observed one and finding the best fit. It is described in Guseva et al. (2006, 2007) and consists of the following. The fit is performed for each SDSS spectrum over the whole observed spectral range of $\lambda\lambda 3900\text{--}9200\text{\AA}$, which includes the Balmer jump region ($\lambda 3646\text{\AA}$) for high-redshift LCGs with $z > 0.1$, and the Paschen jump region ($\lambda 8207\text{\AA}$) for LCGs with $z < 0.12$. As each SED is the sum of both stellar and ionized gas emission, its shape depends on the relative contribution of these two components. In LCGs with high $\text{EW}(\text{H}\beta) > 100\text{\AA}$ (subsamples 1 and 2), the contribution of the ionized gas emission can be very large. However, the equivalent widths of the hydrogen emission lines never reach the theoretical values for pure gaseous emission, which for the $\text{H}\beta$ emission line is $\sim 900 - 1000\text{\AA}$, slightly depending on the electron temperature of the ionized gas. The objects in our LCG sample span a lower range of $\text{EW}(\text{H}\beta)$ s, between 50 and $\sim 500\text{\AA}$ (Fig. 6b), due to the contribution of stellar continuum emission. The contribution of gaseous emission relative to stellar emission can be parameterized by the equivalent width of the $\text{H}\beta$ emission line $\text{EW}(\text{H}\beta)$. Given a temperature $T_e(\text{H}^+)$, the ratio of the gaseous emission to the total emission is equal to the ratio of the observed $\text{EW}(\text{H}\beta)$ to the equivalent width of $\text{H}\beta$ expected for pure gaseous emission. The shape of the spectrum depends also on reddening. The extinction coefficient for the ionized gas $C(\text{H}\beta)_{\text{gas}}$ can be obtained from the observed hydrogen Balmer decrement. However, there is no direct way to derive the extinction coefficient $C(\text{H}\beta)_{\text{stars}}$ for the stellar emission, which can be in principle different from the ionized gas extinction coefficient. Finally, the SED depends on the star formation history of the galaxy.

We have carried out a series of Monte Carlo simulations to reproduce the SED of each galaxy in our sample. To calculate the contribution of the stellar emission to the SEDs, we have adopted the grid of the Padua stellar evolution models by Girardi et al. (2000) with heavy element mass fractions $Z = 0.001, 0.004$, and 0.008 . To reproduce the SED of the stellar component with any star formation history, we have calculated with the package PEGASE.2 (Fioc & Rocca-Volmerange 1997) a grid of instantaneous burst SEDs for a stellar mass of $1 M_\odot$ in a wide range of ages, from 0.5 Myr to 15 Gyr. We have adopted a stellar initial mass function with a Salpeter slope, an upper mass limit of $100 M_\odot$, and a lower mass limit of $0.1 M_\odot$. Then the SED with any star formation history can be obtained by integrating the instantaneous burst SEDs over time with a specified time-varying star formation rate.

We have approximated the star formation history in each LCG by a recent short burst with age $t(\text{young}) < 10$ Myr, which accounts for the young stellar population, and a prior continuous star formation responsible for the older stars, with age starting at $t_2 \equiv t(\text{old})$

and ending at t_1 , with $t_2 > t_1$ and varying between 10 Myr and 15 Gyr. The contribution of each stellar population to the SED is parameterized by the ratio of the masses of the old to young stellar populations, $b = M(\text{old})/M(\text{young})$, which we vary between 0.01 and 1000.

The contribution of the gaseous emission was scaled to the stellar emission using the ratio of the observed equivalent width of the $\text{H}\beta$ emission line to the equivalent width of $\text{H}\beta$ expected for pure gaseous emission. Then the total modeled monochromatic (gaseous+stellar) continuum flux near the $\text{H}\beta$ emission line for a mass of $1 M_\odot$ is scaled to fit the monochromatic extinction-corrected luminosity of the galaxy at the same wavelength. The scaling factor is equal to the total stellar mass M_* in solar units. In our fitting model $M_* = M(\text{young}) + M(\text{old})$, where $M(\text{young})$ and $M(\text{old})$ are respectively the masses of the young and old stellar populations in solar units. These masses are derived using M_* and b .

The SED of the gaseous continuum is taken from Aller (1984) and includes hydrogen and helium free-bound, free-free, and two-photon emission. In our models, it is always calculated with the electron temperature $T_e(\text{H}^+)$ of the H^+ zone and with the chemical composition derived from the H II region spectrum. The observed emission lines corrected for reddening and scaled using the flux of the $\text{H}\beta$ emission line were added to the calculated gaseous continuum. The flux ratio of the gaseous continuum to the total continuum depends on the adopted electron temperature $T_e(\text{H}^+)$ in the H^+ zone, since $\text{EW}(\text{H}\beta)$ for pure gaseous emission decreases with increasing $T_e(\text{H}^+)$. Given that $T_e(\text{H}^+)$ is not necessarily equal to $T_e(\text{O III})$, we chose to vary it in the range $(0.7-1.3) \times T_e(\text{O III})$. Strong emission lines in LCGs (see Fig. 1) are measured with good accuracy, so the equivalent width of the $\text{H}\beta$ emission line and the extinction coefficient for the ionized gas are accurate to 5% and 20%, respectively. Thus, we vary $\text{EW}(\text{H}\beta)$ between 0.95 and 1.05 times its nominal value. As for the extinction, we assume that the extinction coefficient $C(\text{H}\beta)_{\text{stars}}$ for the stellar light is the same as $C(\text{H}\beta)_{\text{gas}}$ for the ionized gas, and we vary both in the range $(0.8-1.2) \times C(\text{H}\beta)$, where $C(\text{H}\beta)$ is the extinction coefficient derived from the observed hydrogen Balmer decrement. For each LCG, we run 10^4 Monte Carlo models varying $t(\text{young})$, t_1 , $t(\text{old})$, b , and $T_e(\text{H}^+)$ randomly in a large range, and $\text{EW}(\text{H}\beta)$ and $C(\text{H}\beta)_{\text{gas}}$ in a relatively smaller range because the latter quantities are more directly constrained by observations. The best modeled SED is found from χ^2 minimization of the deviation between the modeled and the observed continuum in five wavelength ranges which are free of the emission lines.

In Fig. 9a we show the SED fitting of the spectrum of the galaxy J0851+5840 with $\text{EW}(\text{H}\beta) = 303 \text{\AA}$. The total modeled spectrum is labeled “total” while the stellar and gaseous spectra are labeled “stars” and “gas”, respectively. The model SED fits very well the observed spectrum of the galaxy. It is seen that the contribution of gaseous emission is high because of the high $\text{EW}(\text{H}\beta)$. The fraction of the gaseous emission as a function of wavelength in the

spectrum of the same galaxy is shown in Fig. 9b. The two steep jumps seen at $\sim \lambda 3660\text{\AA}$ and $\sim \lambda 8200\text{\AA}$ are respectively due to the Balmer and Paschen discontinuities of the ionized gas emission. Between these jumps, the fraction of gaseous emission increases monotonously from $\sim 20\%$ to $\sim 50\%$ making the spectrum flatter than a pure stellar emission spectrum. Neglecting the contribution of this gaseous emission would have resulted in an artificial increase of the galaxy mass. For the stellar mass determination, we use the SED labeled “stars” in Fig. 9a, which is considerably below the SED labeled “total”.

In Fig. 10, we show the dependence of (a) the absolute g magnitude M_g and (b) of the total stellar mass M_* on the fraction of gaseous continuum near the $H\beta$ emission line. The solid lines are the best linear likelihood fits to the data. It is seen that galaxies with high $\text{EW}(H\beta)$ (filled symbols) are on average fainter and less massive than galaxies with low $\text{EW}(H\beta)$ (open symbols).

5.2. Masses of young and old stellar populations

From the SED fits of the spectra of all the 803 LCGs in our sample, we find the median total stellar mass to be $M_* = 1 \times 10^9 M_\odot$ (Table 1). This value is a factor of ~ 3 lower than the median mass $3 \times 10^9 M_\odot$ found by Cardamone et al. (2009) for their sample of green pea galaxies. As noted before, these star-forming green pea galaxies with their round morphology and high $\text{EW}(H\beta)$ are similar to the LCGs in our subsample 1 which is characterized by an even smaller median mass of $7 \times 10^8 M_\odot$ (Table 1). We believe the factor of ~ 4 in median mass between the Cardamone et al. (2009) green pea sample and our subsample 1 is primarily due to the fact that Cardamone et al. (2009) did not subtract the gaseous continuum emission from the total galaxy emission in deriving their stellar masses. A more detailed comparison between stellar masses derived by us and by Cardamone et al. (2009) is given in Section 5.3.

As for the young stellar population in LCGs, its median mass for the whole sample is $M(\text{young}) = 3 \times 10^7 M_\odot$, i.e. a factor of ~ 30 below the median mass of the old stellar population. There is a small increase of the median mass of the young stellar population by a factor of ~ 1.4 from subsamples 1 and 2 to subsamples 3 and 4 (Table 1). For comparison, the median total stellar mass of LCGs in subsample 1 is ~ 2 times smaller than that in subsample 4.

Fig. 11a shows the dependence of the total stellar mass M_* of LCGs on the mass $M(\text{young})$ of the young stellar population. We note that the total stellar mass is in the range $10^7 - 5 \times 10^{10} M_\odot$, while the mass of the young stellar population is in the range 2×10^6

$-10^9 M_\odot$. Evidently, there is an increase of the mass of the young stellar population with increasing total stellar mass of the galaxy. This suggests that more massive galaxies contain more regions of ongoing star formation. Fig. 11b shows the dependence of the total stellar mass on the ratio b of the mass of the old stellar population to that of the young stellar population. It is seen that $M(\text{old})/M(\text{young})$ increases with increasing M_* , reaching the high values of several hundreds, predominantly in galaxies with low $\text{EW}(\text{H}\beta)$ (open symbols). On the other hand, there is an appreciable number of LCGs with high $\text{EW}(\text{H}\beta)$ and low $M(\text{old})/M(\text{young})$ (filled symbols), implying that less massive dwarf galaxies ($10^7 M_\odot \lesssim M_* \lesssim 10^8 M_\odot$) are also less evolved, both in terms of their stellar populations and metallicities.

In the fitting analysis and in the determination of global characteristics of LCGs such as luminosities and masses, we have made no correction for aperture effects. Yet, these effects can be important, especially for galaxies at low redshifts, which may have angular sizes larger than the $3''$ diameter of the fibers with which the SDSS spectra were obtained. We estimate these aperture corrections below. Assuming that the spectral energy distribution in the galaxy inside and outside the round aperture are the same, the aperture correction factor can be written as

$$f(\text{apcorr}) = 10^{0.4(r(3'')-r(\text{tot}))}, \quad (2)$$

where $r(3'')$ and $r(\text{tot})$ are respectively the SDSS r apparent magnitude inside the $3''$ round aperture and the modeled integrated SDSS r apparent magnitude of the galaxy as derived from the SDSS images. Both $r(3'')$ and $r(\text{tot})$ are taken from the SDSS DR7 database. Using Eq. 2, we found the median flux correction factor $f(\text{apcorr})$ to vary from ~ 1.4 for subsample 1 to ~ 1.8 for subsample 4. However, for comparison purposes, we have decided not to apply these aperture corrections to the LCG sample, as they are not taken into account in other studies. Furthermore, the assumption that the spectral energy distributions of the galaxy inside and outside the slit are the same may not be valid. Thus, we should keep in mind that the true global characteristics for LCGs, such as luminosity, mass or star formation rate, may be larger than those derived here from the galaxy spectra, especially for nearby galaxies.

5.3. Comparison of stellar masses and oxygen abundances of green pea galaxies derived by us and by Cardamone et al. (2009)

As discussed before, there are 66 green pea galaxies from Cardamone et al. (2009) that are included in the LCG sample. We compare here their stellar masses and oxygen abundances derived by us to those obtained by Cardamone et al. (2009). We show in Table 2 the SDSS ID number of each galaxy, its equatorial coordinates, its stellar masses and

oxygen abundances derived by Cardamone et al. (2009) and in this paper. An examination of the Table shows that the stellar masses of green pea galaxies derived in this paper are systematically lower than those obtained by Cardamone et al. (2009). This effect is also clearly seen in Fig. 12a. As already discussed, this systematic offset is due to the fact that, in fitting the SED, we subtract the contribution of gaseous continuum emission, which results in lower stellar masses. This effect is largest for lower-mass galaxies with $\log M_*/M_\odot \lesssim 8.5$. These are mostly galaxies with high $\text{EW}(\text{H}\beta)$ in subsample 1.

Fig. 12b shows the comparison of oxygen abundances for the same galaxies. Again, the Cardamone et al. (2009) abundances are systematically larger (~ 0.6 dex in $12+\log\text{O}/\text{H}$) than ours. This systematic offset is a consequence of the different abundance determination methods used, the more uncertain strong-line method by Cardamone et al. (2009), and the more reliable direct method by us. We note that nearly all abundance determinations in high-redshift galaxies and in the majority of nearby SDSS star-forming galaxies are based on strong-line methods. The more uncertain oxygen abundances that result from these methods should not be used in galaxy evolution studies without a careful analysis of their errors.

6. Younger starbursts are hotter and denser than older ones

We investigate here how the properties of the luminous H II regions in LCGs depend on the stellar mass of the galaxy. In particular, we examine the dependence of the electron temperature $T_e(\text{O III})$ and the electron number density $N_e(\text{S II})$ on the total stellar mass M_* of the galaxy (respectively Figs. 13a and 13b). We find that both the electron temperature and the electron number density are systematically higher in galaxies with higher $\text{EW}(\text{H}\beta)$. These galaxies also have systematically lower masses. The median electron temperatures and electron number densities of the galaxies in the different LCG subsamples vary from 13 100K and 180 cm^{-3} in subsample 1, to 11 700K and 90 cm^{-3} in subsample 4.

Young stellar populations in galaxies with higher $\text{EW}(\text{H}\beta)$ have younger ages $t(\text{young})$ (Table 1). Thus, we conclude that the younger starbursts in our LCGs are systematically hotter and denser.

7. Mass-metallicity relation

In Fig. 14a,b we show the mass-metallicity relation for LCGs. It is seen that galaxies with lower mass have systematically lower oxygen abundances. These lower-mass galaxies are primarily from subsamples 1 and 2 with high $\text{EW}(\text{H}\beta)$, while LCGs with lower $\text{EW}(\text{H}\beta)$

are higher-mass objects with higher oxygen abundance. Although there is a large scatter, the data can be fitted by a linear relation, shown in Fig. 14a by a solid line

$$12 + \log \text{O}/\text{H} = (7.475 \pm 0.426) + (0.069 \pm 0.047) \times \log M_*, \quad (3)$$

where M_* is in solar units. We also show by a dashed line in Figure 14a the polynomial fit obtained by Amorín et al. (2010) to the green pea galaxy sample of Cardamone et al. (2009). The difference between our fit and that of Amorín et al. (2010) is due to the fact that we take into account the gaseous continuum emission and thus derived lower stellar masses producing an offset by a factor of ~ 4 in the galaxy mass between our data and Amorín et al. (2010) fit. Furthermore, because of a small stellar mass range and a large dispersion in oxygen abundances, there is no strong evidence from Fig. 3 of Amorín et al. (2010) that the data for green pea galaxies is better fit by a polynomial than a line. A linear fit to the Amorín et al. (2010) data would result in a better agreement with the fit to LCGs derived in this paper.

We show by a dash-dotted line the fit of Amorín et al. (2010) to a sample of star-forming galaxies assembled from the SDSS. This relation is considerably steeper than the one obtained for LCGs. The difference is probably not due to the determination of the stellar masses of the SDSS star-forming galaxies. The equivalent width of their $\text{H}\beta$ emission line is generally small, so that ionized gas emission is small. However, the oxygen abundances of these galaxies are derived using strong-line empirical methods which produce a systematic offset as compared to the oxygen abundances derived by the direct method. That is probably why the relations for SDSS star-forming galaxies and LCGs differ.

The relation shown by the solid line in Fig. 14a is also at odds with the finding of Cardamone et al. (2009) for their green pea sample. Those authors did not find a clear evidence for the dependence of the oxygen abundance on stellar mass. This is likely because of the way they derive the metallicities and masses of their galaxies. As discussed before, oxygen abundances were derived by using the more uncertain strong-line technique, and stellar masses were determined without subtracting the gaseous continuum emission from the observed SED. In that way, both oxygen abundances and galaxy stellar masses are overestimated. Another reason for why a mass-metallicity relation was not seen by Cardamone et al. (2009) is probably because the $10^8 - 10^{10.5} M_\odot$ mass range of their sample is smaller than the $10^7 - 10^{10.5} M_\odot$ mass range of our LCG sample.

In contrast to Fig. 14a, Fig. 14b shows that the N/O abundance ratio for LCGs with $\text{EW}(\text{H}\beta) \geq 100\text{\AA}$ (filled symbols) is independent on stellar mass, implying a primary origin for nitrogen in these galaxies. As for LCGs with $\text{EW}(\text{H}\beta) < 100\text{\AA}$ (open symbols), there is a dependence of N/O ratio on the total galaxy mass, implying some secondary nitrogen production in the highest-mass galaxies.

8. Star formation rate

One of the most important characteristics governing a galaxy’s evolution is its star formation rate. We derive the star formation rate $\text{SFR}(\text{H}\alpha)$, using the extinction-corrected luminosity $L(\text{H}\alpha)$ of the $\text{H}\alpha$ emission line and the star formation rate $\text{SFR}(\text{FUV})$, using the extinction-corrected GALEX FUV luminosity $L(\text{FUV})$, and relations given by Kennicutt (1998)

$$\text{SFR}(\text{H}\alpha) = 7.9 \times 10^{-42} L(\text{H}\alpha), \quad (4)$$

$$\text{SFR}(\text{FUV}) = 1.4 \times 10^{-28} L(\text{FUV}). \quad (5)$$

In equations 4 and 5, SFR is in units of $M_\odot \text{ yr}^{-1}$, $L(\text{H}\alpha)$ in erg s^{-1} and $L(\text{FUV})$ in $\text{erg s}^{-1} \text{ Hz}^{-1}$. To correct $L(\text{FUV})$ for extinction we adopt the reddening law of Cardelli et al. (1989) with $R = A(V)/E(B - V) = 3.1$ and the extinction coefficient $C(\text{H}\beta)$ derived from the optical SDSS spectrum. Then the extinction correction factor for $L(\text{FUV})$ is equal to $2.512^{A(\text{FUV})}$ with $A(\text{FUV}) = 8.24 \times E(B - V) = 5.58 \times C(\text{H}\beta)$.

The GALEX FUV fluxes are available for 675 galaxies out of the 803 LCGs in our sample. In Table 1, we give the median $\text{SFR}(\text{H}\alpha)$ and $\text{SFR}(\text{FUV})$ for the different subsamples and for the total sample. It can be seen that the $\text{SFR}(\text{H}\alpha)$ and $\text{SFR}(\text{FUV})$ are in good agreement and that their median values do not change appreciably from one subsample to the next, being $\sim 4 M_\odot \text{ yr}^{-1}$. Because of the good agreement, we will consider below only SFRs derived from the $\text{H}\alpha$ luminosity.

In Fig. 15a we show the dependence of $\text{SFR}(\text{H}\alpha)$ on the total stellar mass M_* . The star formation rate for LCGs is in the range 0.7 - 60 $M_\odot \text{ yr}^{-1}$. The median values in different subsamples are in the narrow range 3.4 – 5.0 $M_\odot \text{ yr}^{-1}$ (Table 1). Thus, there is no significant difference in the average SFR for galaxies with different $\text{EW}(\text{H}\beta)$. However, we note the increase of $\text{SFR}(\text{H}\alpha)$ with increasing total stellar mass in galaxies from subsamples 3 and 4 (galaxies with $\text{EW}(\text{H}\beta) < 100\text{\AA}$ shown in Fig. 15a by open symbols), while there is a less strong dependence for galaxies from subsamples 1 and 2 (galaxies with $\text{EW}(\text{H}\beta) \geq 100\text{\AA}$ shown in Fig. 15a by filled symbols). The range of SFRs in LCGs is comparable to that in the intermediate-redshift star-forming galaxies (Hoyos et al. 2005; Kakazu et al. 2007) and in LBGs (Pettini et al. 2001), but is ~ 10 -100 times higher than in typical nearby BCDs. For example, the SFR in the prototype BCD I Zw 18 is 0.1 $M_\odot \text{ yr}^{-1}$ (Thuan 2008).

The dependence of the specific star formation rate $\text{SSFR}(\text{H}\alpha) = \text{SFR}(\text{H}\alpha)/M_*$ is shown in Fig. 15b. The SSFR is of interest because it is related to the time needed to double the stellar mass of a galaxy. We show by dashed lines from left to right the loci of constant star formation corresponding to 1, 10 and 100 $M_\odot \text{ yr}^{-1}$, respectively. It is seen that there is an inverse dependence of the SSFR on the total stellar mass of LCGs. The lowest SSFRs

($\sim 10^{-9} \text{ yr}^{-1}$) occur in the highest-mass galaxies with $\text{EW}(\text{H}\beta) < 100\text{\AA}$, while the highest SSFRs (up to $\sim 10^{-7} \text{ yr}^{-1}$) are found almost exclusively in galaxies with $\text{EW}(\text{H}\beta) \geq 100\text{\AA}$. These values are very high, higher than those found by Cardamone et al. (2009) for their green pea galaxies (their maximum SSFRs are $\sim 10^{-8} \text{ yr}^{-1}$), mainly because those authors overestimated the galaxy stellar masses. They are also considerably higher than those found in merging galaxies which lie in the $10^{-10} \text{ yr}^{-1} - 10^{-9} \text{ yr}^{-1}$ range. Our SSFR values are comparable to those found in high-redshift galaxies in the ranges $z = 4-6$ (Stark et al. 2009) and $6-8$ (Schaerer & de Barros 2010). Thus, our LCGs resemble galaxies with the highest SSFR known.

The quantity $1/\text{SSFR}(\text{H}\alpha)$ is also a measure of the time needed to double the metallicity of a galaxy. Thus, if a constant star formation rate is assumed, then the ISM in our galaxies is enriched by heavy elements on a time scale of $\sim 10^7 - 10^9 \text{ yr}$, considerably smaller than the Hubble time. It is likely then that star formation in LCGs proceeds in short bursts of duration $10^6 - 10^7 \text{ yr}$. Then, the SSFR averaged over time would be much lower. Bursts of star formation separated by long quiescent periods of several Gyr (not unlike the situation in BCDs, see Thuan 2008) are also required in the LCGs with the highest SFRs, so as not to exhaust the gas supply for star formation. Assuming continuous star formation, then with a hydrogen gas supply of $10^{10} M_{\odot}$ and a SFR of $50 M_{\odot} \text{ yr}^{-1}$, the time for gas depletion is only $\sim 2 \times 10^8 \text{ yr}$. Clearly a burst mode is required for the LCGs with the highest SFRs.

9. Age of stellar populations and the burst mode of star formation in LCGs

While the young stellar population in our galaxies is modeled by a short burst occurring at $t(\text{young}) \sim 3 - 4 \text{ Myr}$ (Table 1), the older stellar population is fitted by a model with continuous star formation starting at $t_2 \equiv t(\text{old})$ and ending at t_1 , with $t_2 > t_1$. The parameter $t(\text{old})$ sheds light on the evolutionary status of the galaxy (whether the galaxy is young or old), and helps to understand the character of its star formation (whether it proceeds in a bursting or continuous manner).

Fig. 16 shows how the age of the oldest stellar population $t(\text{old})$ depends on the total stellar mass M_* . The dashed lines are the loci of constant continuous star formation rate corresponding to, from left to right, $\text{SFR} = 1, 10 \text{ and } 100 M_{\odot} \text{ yr}^{-1}$.

It can be seen that galaxies with high $\text{EW}(\text{H}\beta)$ ($\geq 100\text{\AA}$) denoted by filled symbols do not show any evident trend. On the other hand, there is an increase of $t(\text{old})$ with increasing M_* for galaxies with $\text{EW}(\text{H}\beta) < 100\text{\AA}$. This implies that, among the galaxies with low $\text{EW}(\text{H}\beta)$, massive galaxies are in general older than lower mass galaxies. The

absence of such a dependence for galaxies with high $\text{EW}(\text{H}\beta)$ may in part be explained by the uncertainties in the SED modeling. Indeed, the fraction of the light produced by the old stellar population in spectra of galaxies with a high $\text{EW}(\text{H}\beta)$ is much lower than that in galaxies with a low $\text{EW}(\text{H}\beta)$, both because of the brighter young stellar population and of the higher contribution of gaseous emission. Furthermore, galaxies with high $\text{EW}(\text{H}\beta)$ have systematically higher redshifts compared to galaxies with low $\text{EW}(\text{H}\beta)$. Their larger distances make their continua weaker, which renders their SED fitting more uncertain. This is because of the following selection effect. We select only galaxies with $[\text{O III}] \lambda 4363$ that can be measured with good accuracy for abundance determination, and this line is stronger in galaxies with high $\text{EW}(\text{H}\beta)$.

The location of the galaxies in Fig. 16 relative to the dashed lines indicates continuous SFRs that are somewhat lower than the ongoing SFRs derived by equations 4 and 5, and shown in Fig. 15a. The largest offset is for low-mass galaxies with high $\text{EW}(\text{H}\beta)$ (filled symbols). The vast majority of these galaxies are located in the region corresponding to continuous SFRs $< 1 M_{\odot} \text{ yr}^{-1}$, i.e. $\gtrsim 10$ times lower than those derived from the ongoing star formation episode. This discrepancy is again an indication that star formation in the LCGs occurs in rare bursts of short duration, so that the SFR averaged over the lifetime of the galaxy is more than one order of magnitude lower than the one derived from the $\text{H}\alpha$ luminosity. The bursting nature of star formation is less pronounced for the higher-mass galaxies with low $\text{EW}(\text{H}\beta)$ (open symbols): their continuous SFRs averaged over the galaxy’s lifetime are only $\sim 2 - 3$ times lower than those derived from the ongoing episode of star formation.

10. Conclusions

We discuss here the properties of a sample of luminous compact star-forming galaxies (LCG) selected from the Data Release 7 (DR7) of the Sloan Digital Sky Survey (SDSS). We show that the so-called “green pea” galaxies discussed by Cardamone et al. (2009) are a subset of these LCGs. However, in contrast to Cardamone et al. (2009) who selected their green pea galaxies solely on the basis of broad-band SDSS colors and compact structure, our LCG galaxies were chosen also on the basis of their spectroscopic properties. Our main selection criteria are as follows: a) a high extinction-corrected luminosity $L(\text{H}\beta) > 3 \times 10^{40} \text{ erg s}^{-1}$ of the $\text{H}\beta$ emission line; b) a high equivalent width $\text{EW}(\text{H}\beta) \geq 50 \text{ \AA}$ of the $\text{H}\beta$ emission line; c) a strong $[\text{O III}] \lambda 4363$ emission line allowing accurate abundance determination; d) a compact structure on SDSS images; and e) an absence of obvious AGN spectroscopic features. Using these criteria, we selected in total 803 galaxies, split into four subsamples

based on the value of $\text{EW}(\text{H}\beta)$ (greater or smaller than 100\AA) and morphological appearance (round shape or some evidence of disturbed morphology).

Analysis of the LCG sample has led to the following findings:

1. The selected galaxies have redshifts between 0.02 and 0.63, a redshift range that is a factor $\gtrsim 2$ higher than the redshift range $z = 0.112 - 0.360$ of the green pea sample of Cardamone et al. (2009). We find that the properties of LCGs and green pea galaxies selected from the SDSS are in many respects similar to those of well-studied nearby luminous blue compact dwarf (BCD) galaxies, such as SBS 0335–052E and HS 0837+4717. Since the color of an emission-line galaxy on the *gri* SDSS composite image changes with its redshift, depending on which strong emission lines fall within a particular filter band, the LCGs display a variety of colors from intense blue for nearby galaxies with $z < 0.07$, through pink and green at redshifts $z \sim 0.09$ and $\sim 0.15 - 0.30$, respectively, to brown at redshifts $z \sim 0.6$. Therefore, the green pea galaxy sample is just a subsample with a narrow redshift range of a larger LCG sample. A significant fraction of our LCGs have low redshifts ($z < 0.1$), thus allowing the study of LCG properties in more detail than in the previous investigations of Cardamone et al. (2009) and Amorín et al. (2010).

2. Although our selection criteria do not set an upper limit on the luminosity $L(\text{H}\beta)$ of the $\text{H}\beta$ emission line, we find that there is an upper bound to $L(\text{H}\beta)$ at $\sim 3 \times 10^{42} \text{ erg s}^{-1}$. This implies a self-regulating mechanism of star formation that does not allow the formation of star-forming regions brighter than that limit in a galaxy.

3. In the $[\text{O III}] \lambda 5007/\text{H}\beta$ vs $[\text{N II}] \lambda 6583/\text{H}\alpha$ diagnostic diagram, LCGs occupy the region of star-forming galaxies with the highest excitation. On the other hand, the five low-metallicity AGNs discovered by Izotov et al. (2007, 2010) and Izotov & Thuan (2008) also lie in the same region. This implies that further detailed studies of LCGs may result in the discovery of a larger number of low-metallicity AGNs showing some Seyfert 1 features such as broad hydrogen emission lines.

4. We find that the oxygen abundances $12 + \log \text{O}/\text{H}$ in LCGs are in the range $7.6 - 8.4$ with a median value of ~ 8.11 , confirming the results of Amorín et al. (2010) concerning a subset of the green pea sample of Cardamone et al. (2009). This range of oxygen abundances is typical of nearby lower-luminosity BCDs. We note, however, that the median oxygen abundance of ~ 8.7 , derived by Cardamone et al. (2009) for their green pea sample is overestimated, because those authors used empirical relations for abundance determinations, instead of the direct method used in this paper and in Amorín et al. (2010). There is no dependence of $12 + \log \text{O}/\text{H}$ on redshift. On the other hand, we find that the oxygen abundances in galaxies with higher equivalent width $\text{EW}(\text{H}\beta)$ are generally lower.

As for the N/O, Ne/O, S/O, Cl/O, Ar/O and Fe/O abundance ratios, they are similar to those found for lower-luminosity BCDs. Overall, we find no appreciable difference in element abundances between LCGs and BCDs, implying a similar chemical enrichment history.

5. In the luminosity-metallicity diagram, LCGs are shifted by ~ 2 mag to brighter magnitudes as compared to the bulk of nearby emission-line galaxies. However, together with the most metal-deficient nearby BCDs I Zw 18, SBS 0335–052W, SBS 0335–052E, extremely metal-poor intermediate-redshift galaxies ($z < 1$, Kakazu et al. 2007), luminous compact metal-poor galaxies ($z \sim 0.7$, Hoyos et al. 2005) and Lyman-break galaxies (LBG) ($z \sim 3$, Pettini et al. 2001), LCGs form a common luminosity-metallicity relation, that for the most actively star-forming galaxies. Some LCGs have oxygen abundances and luminosities similar to LBGs, despite much lower redshifts. This opens the possibility of studying LBGs through brighter and hence easier to observe LCGs.

6. We develop a technique for determining galaxy masses by fitting the observed spectral energy distribution (SED) by a model SED that includes both emission from stellar populations of different ages and the continuum emission from the ionized gas, the latter having not been considered by previous investigators. We show that such an omission results in an overestimate of the stellar mass. This effect is especially strong for galaxies with high $\text{EW}(\text{H}\beta) > 100\text{\AA}$. Thus, the median mass of the galaxies in our sample is a factor of ~ 3 times lower than that derived by Cardamone et al. (2009) and used by Amorín et al. (2010).

7. The total stellar mass of LCGs is in the range $\sim 10^7 - \sim 10^{11} M_{\odot}$, with a median value of $\sim 10^9 M_{\odot}$. The median mass of $\sim 3 \times 10^7 M_{\odot}$ of the young stellar population is a factor of ~ 30 lower. We find that the mass of the young stellar population increases with increasing total stellar mass. However, the fraction by mass of the young stellar population is higher in galaxies with a low total stellar mass. Furthermore, H II regions in low-mass LCGs are systematically hotter and denser, than those in high-mass galaxies.

8. We find a clear increase of the oxygen abundance with increasing total stellar mass of the galaxy in the mass-metallicity diagram. However, there is no correlation between the N/O abundance ratio and the total stellar mass for the lowest-mass galaxies, those with $\text{EW}(\text{H}\beta) \geq 100\text{\AA}$, implying primary N production in those objects. There is however a total mass dependence of N/O for the highest-mass galaxies, those with $\text{EW}(\text{H}\beta) < 100\text{\AA}$, implying some secondary of N in those galaxies.

9. The star formation rate in LCGs varies in a large range $\sim 0.7 - \sim 60 M_{\odot} \text{ yr}^{-1}$ with a median value of $\sim 4 M_{\odot} \text{ yr}^{-1}$. The range and median value of the SFRs in LCGs is lower by a factor of several, as compared to Lyman-break galaxies at redshift ~ 3 (Pettini et al. 2001)

and higher-redshift galaxies (Stark et al. 2009; Schaerer & de Barros 2010). However, the highest SFRs found in LCGs compare well with those in high-redshift galaxies. LCGs have specific star formation rates that are among the highest known, in the range $\sim 10^{-7} - 10^{-9}$ yr^{-1} , and comparable to those of high-redshift galaxies in the $z \sim 3 - 8$ redshift range. This similarity offers the possibility of studying extreme star formation in high-redshift galaxies by using LCGs as relatively nearby proxies.

10. We find that the age of the oldest stellar population increases with increasing stellar mass in the LCGs with low $\text{EW}(\text{H}\beta)$ ($< 100\text{\AA}$). However, no such dependence is found for galaxies with high $\text{EW}(\text{H}\beta)$, an absence which can be explained by larger uncertainties in fitting the spectra of these galaxies. Star formation in LCGs at the rate derived from $\text{H}\alpha$ emission cannot be continuous, but rather must occur in strong short bursts separated by long quiescent phases, just as in BCDs. The bursting nature of star formation is more pronounced in LCGs with higher $\text{EW}(\text{H}\beta)$ and lower masses.

Y.I.I. is grateful to the staff of the Astronomy Department at the University of Virginia for their warm hospitality. Support for this work is provided by NASA. Y.I.I. and N.G.G. acknowledge the support of the Cosmomicrophysics project of the National Academy of Sciences of Ukraine. Funding for the Sloan Digital Sky Survey (SDSS) and SDSS-II has been provided by the Alfred P. Sloan Foundation, the Participating Institutions, the National Science Foundation, the U.S. Department of Energy, the National Aeronautics and Space Administration, the Japanese Monbukagakusho, and the Max Planck Society, and the Higher Education Funding Council for England.

REFERENCES

- Abazajian K. N., et al., 2009, *ApJS*, 182, 543
- Aller, L. H. 1984, *Physics of Thermal Gaseous Nebulae* (Dordrecht: Reidel)
- Amorín, R. O., Pérez-Montero, E., & Vílchez, J. M. 2010, *ApJ*, 715, L128
- Asplund, M., Grevesse, N., Sauval, A.J., & Scott, P. 2009, *ARA&A*, 47, 481
- Baldwin, J. A., Phillips, M. M., & Terlevich, R. 1981, *PASP*, 93, 5
- Cardamone, C., et al. 2009, *MNRAS*, 399, 1199
- Cardelli, J. A., Clayton, G. C., & Mathis, J. S. 1989, *ApJ*, 345, 245

- Fioc, M., & Rocca-Volmerange, B. 1997, *A&A*, 326, 950
- Girardi, L., Bressan, A., Bertelli, G., & Chiosi, C. 2000, *A&AS*, 141, 371
- González Delgado, R. M., Cerviño, M., Martins, L. P., Leitherer, C., & Hauschildt, P. H. 2005, *MNRAS*, 357, 945
- Guseva, N. G., Izotov, Y. I., & Thuan, T. X. 2006, *ApJ*, 644, 890
- Guseva, N. G., Izotov, Y. I., Papaderos, P., & Fricke, K. J. 2007, *A&A*, 464, 885
- Guseva, N. G., Papaderos, P., Meyer, H. T., Izotov, Y. I., & Fricke, K. J. 2009, *A&A*, 505, 63
- Hoyos, C., Koo, D. C., Phillips, A. C., Willmer, C. N. A., & Guhathakurta, P. 2005, *ApJ*, 635, L21
- Izotov, Y. I., & Thuan, T. X. 2008, *ApJ*, 687, 133
- Izotov, Y. I., & Thuan, T. X. 2004, *ApJ*, 602, 200
- Izotov, Y. I., Guseva, N. G., Lipovetsky, V. A., Kniazev, A. Y., & Stepanian, J. A. 1990 *Nature*, 343, 238
- Izotov, Y. I., Thuan, T. X., & Lipovetsky, V. A. 1994, *ApJ*, 435, 647
- Izotov, Y. I., Lipovetsky, V. A., Chaffee, F. H., Foltz, C. B., Guseva, N. G., & Kniazev, A. Y. 1997, *ApJ*, 476, 698
- Izotov, Y. I., Stasińska, G., Meynet, G., Guseva, N. G., & Thuan T. X. 2006, *A&A*, 448, 955
- Izotov, Y. I., Thuan, T. X., & Guseva, N. G. 2007, *ApJ*, 671, 1297
- Izotov, Y. I., Guseva, N. G., Fricke, K. J., Stasińska, G., Henkel, C., & Papaderos, P. 2010, *A&A*, in press; preprint arXiv:1005.1844
- Kakazu, Y., Cowie, L. L., & Hu, E. M. 2007, *ApJ*, 668, 853
- Kauffmann, G., Heckman, T. M., Tremonti, C., et al. 2003, *MNRAS*, 346, 1055
- Kennicutt, R. C., Jr. 1998 *ARA&A*, 36, 189
- Lintott, C. J., Schawinski, K., Slosar, A., et al. 2008, *MNRAS*, 389, 1179
- Lintott, C. J., Schawinski, K., Bamford, S., et al. 2011, *MNRAS*, 410, 166

- Pettini, M., Shapley, A. E., Steidel, C. C., et al. 2001, *ApJ*, 554, 981
- Pustilnik, S., Kniazev, A., Pramskij, A., Izotov, Y., Foltz, C., Brosch, N., Martin, J.-M., & Ugryumov, A. 2004, *A&A*, 419, 469
- Schaerer, D., & de Barros, S. 2010, *A&A*, 515, 73
- Schneider, D. P., et al. 2010, *AJ*, 139, 2360
- Stark, D. P., Ellis, R. S., Bunker, A., Bundy, K., Targett, T., Benson, A., & Lacy, M. 2009, *ApJ*, 697, 1493
- Stasińska G., Cid Fernandes R., Mateus A., Sodré L., & Asari N. V., 2006, *mnras*, 371, 972
- Thuan, T. X. 2008, in *Low-metallicity star formation: from the first stars to dwarf galaxies*, ed. L. Hunt, S.C. Madden, & R. Schneider (Cambridge: Cambridge Univ. Press), 348
- Thuan, T. X., & Izotov, Y. I. 2005, *ApJS*, 161, 240
- Thuan, T. X., Izotov, Y. I., & Lipovetsky, V. A. 1997, *ApJ*, 477, 661
- Tremonti, C. A., Heckman, T. M., Kauffmann, G., et al. 2004, *ApJ*, 613, 898
- Whitford, A. E. 1958, *AJ*, 63, 201

Table 1. Average characteristics of LCGs

Sample	z	g	$E(B - V)$	M_{total} $10^9 M_{\odot}$	M_{young} $10^7 M_{\odot}$	t_{young} Myr
1	0.201	20.3	0.10	0.68	2.87	3.0
2	0.129	19.3	0.12	0.64	2.37	3.3
3	0.152	19.2	0.12	1.31	3.86	4.4
4	0.094	18.4	0.15	1.39	3.62	4.0
Total	0.116	18.9	0.13	1.07	3.12	3.6
Sample	$T_e(\text{O III})$ K	$N_e(\text{S II})$ cm^{-3}	$12+\log\text{O/H}$	$\text{SFR}(\text{H}\alpha)$ $M_{\odot} \text{ yr}^{-1}$	$\text{SFR}(\text{FUV})$ $M_{\odot} \text{ yr}^{-1}$	
1	13100	180	8.04	5.0	3.4	
2	12400	130	8.09	4.1	3.3	
3	12200	120	8.09	4.3	4.0	
4	11700	90	8.16	3.4	4.5	
Total	12200	110	8.11	4.1	3.9	

Table 2. Characteristics of Cardamone et al. (2009) Green Pea galaxies included in the LCG sample

SDSS ID	RA J2000	Dec J2000	Cardamone et al. (2009)		this paper	
			12+logO/H	log(M_*/M_\odot)	12+logO/H	log(M_*/M_\odot)
588848899919446344	195.546460	−0.087897	8.75	9.08	8.12	9.02
587725576962244831	261.776373	59.817273	8.71	9.81	8.24	9.26
587731187273892048	351.413453	0.752012	8.70	9.38	8.29	9.41
587727179006148758	45.839226	−7.989791	8.71	8.75	7.86	9.15
587724240158589061	54.949128	−7.428132	8.78	9.75	8.38	9.70
587726032253419628	191.097382	2.261231	8.70	9.45	8.17	9.65
588010360138367359	130.570630	3.635203	8.55	9.71	8.19	9.38
587726102030451047	236.787938	3.603914	8.74	8.96	8.16	8.79
587729155743875234	173.265848	65.228162	8.66	10.05	7.97	9.30
587728919520608387	212.938906	62.653138	8.67	10.18	8.20	9.09
587729229297090692	234.405309	58.794575	8.58	9.27	8.04	9.16
587730774416883967	339.396081	13.613062	8.55	10.10	8.16	9.45
587730774965354630	6.716985	15.460460	8.81	9.58	8.07	9.02
587728906099687546	117.403215	33.621219	8.79	9.85	8.29	9.49
587725550133444775	156.563375	63.552363	...	9.05	8.09	8.23
588009371762098262	170.582224	61.912629	8.70	8.71	8.29	7.85
588011122502336742	181.772142	61.586621	...	9.85	8.09	8.38
588013384341913605	141.501678	44.460044	8.62	9.08	8.01	8.78
587732134315425958	195.368010	51.080893	8.63	9.53	8.00	9.98
587729777439801619	204.299529	−2.434842	8.76	9.94	8.26	9.19
587729777446945029	220.630713	−2.164466	8.57	8.80	7.94	8.65
587732152555864324	116.991682	23.609113	...	9.40	7.98	9.06
587732578845786234	157.912214	7.265701	8.52	9.02	8.33	8.75
587733080270569500	163.378431	52.631353	8.78	9.75	8.10	9.77
588297864714387604	131.975356	33.615227	8.81	9.50	8.02	9.37
587735696987717870	213.630037	54.515587	8.58	8.81	7.94	8.02
587733441055359356	251.527242	31.514859	...	8.76	8.03	9.07
588017605211390138	154.513517	41.105860	8.68	9.82	7.82	9.32
588017114517536797	216.023868	42.279524	8.78	9.00	8.04	8.34
588017116132540589	228.535985	38.868716	...	8.90	8.40	9.32
588018090541842668	235.755108	34.767079	...	8.76	8.00	8.05
588018090013098618	251.898063	22.783002	8.61	9.27	8.06	8.76
588016878295515268	137.879799	31.457439	...	9.27	7.94	8.37
587735661007863875	139.260529	31.872384	8.95	9.44	8.34	9.37
588018055114784812	220.041419	46.326930	8.72	9.83	8.09	9.62
588018055652769997	223.648271	45.482288	8.84	10.22	8.11	9.52

Table 2—Continued

SDSS ID	RA J2000	Dec J2000	Cardamone et al. (2009)		this paper	
			12+logO/H	log(M_*/M_\odot)	12+logO/H	log(M_*/M_\odot)
588017570848768137	192.144310	12.567480	8.53	9.06	8.11	9.05
587736915687964980	241.152768	8.333082	8.75	9.90	8.02	8.48
587736915687375248	239.858241	8.688655	8.64	8.74	8.07	8.97
587738410863493299	152.987850	13.139471	8.64	8.66	8.01	8.31
587735349111947338	184.766599	15.435698	8.82	8.66	7.89	8.35
587738570859413642	204.867933	15.278369	8.83	9.96	8.09	9.43
587736940372361382	217.614622	34.154720	...	9.31	7.99	8.75
587739153352229578	117.990764	16.637010	8.65	9.96	7.87	8.35
587738947196944678	123.966679	21.939902	8.55	8.72	8.00	8.71
587738371672178952	125.698590	22.695578	8.81	9.33	8.08	8.43
588017978880950451	150.556494	34.704908	8.64	9.58	8.01	8.52
587739408388980778	174.342249	35.407413	8.76	9.32	8.16	9.56
588017977277874181	171.657352	38.050810	8.56	9.79	8.04	8.83
587739406242742472	178.020352	34.013853	...	8.86	7.96	8.35
587739828742389914	224.396405	22.533833	8.55	9.30	8.04	9.13
587739652107600089	238.041673	21.053410	8.68	9.90	7.91	9.46
587739721387409964	249.330431	14.651378	8.62	9.64	8.30	9.41
587741600420003946	181.252807	26.346595	8.81	9.66	8.23	9.84
587741421099286852	126.715863	18.347732	8.75	8.67	8.23	8.81
587741532770074773	133.350354	19.506280	8.68	9.37	8.13	9.32
587741817851084830	137.805603	18.518936	8.89	9.93	8.00	9.75
587741392649781464	152.329151	29.272638	8.69	8.55	7.91	7.87
587741490367889543	158.112322	27.298680	8.69	10.02	8.22	9.65
587742014876745993	141.869487	17.671838	8.51	9.38	8.01	9.26
588023240745943289	140.705287	19.227629	8.59	10.48	8.30	9.56
587745243087372534	141.384863	14.053623	8.73	9.08	7.94	8.46
587744874785145599	121.325174	9.425978	...	10.24	8.28	9.36
587742013825941802	197.653081	21.804731	8.83	9.27	8.54	9.46
587742062151467120	196.734804	22.694003	...	10.10	8.02	9.82
587741727655919734	193.761316	25.935911	...	10.02	8.10	9.45

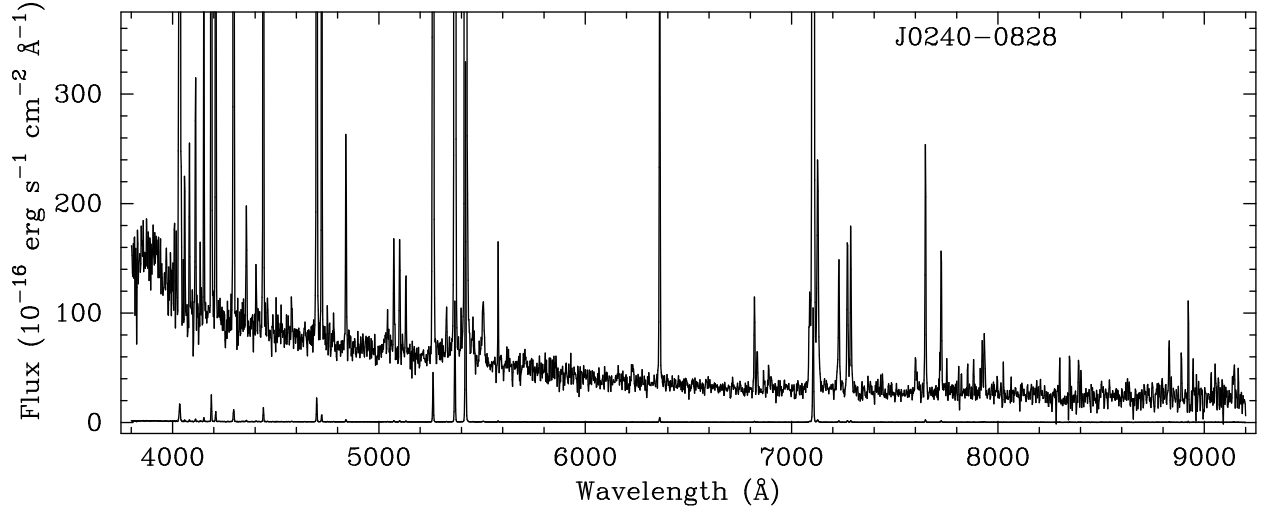


Fig. 1.— SDSS spectrum of a luminous compact emission-line galaxy in our sample obtained with the 2.5m Apache Point Observatory Sloan telescope in a 1h exposure. The ordinate scale is for the lower spectrum. The upper spectrum is the lower spectrum expanded by a factor of 100 along the ordinate. Weak emission lines with fluxes of $\sim 1\%$ that of $\text{H}\beta$ are clearly detected in this spectrum.

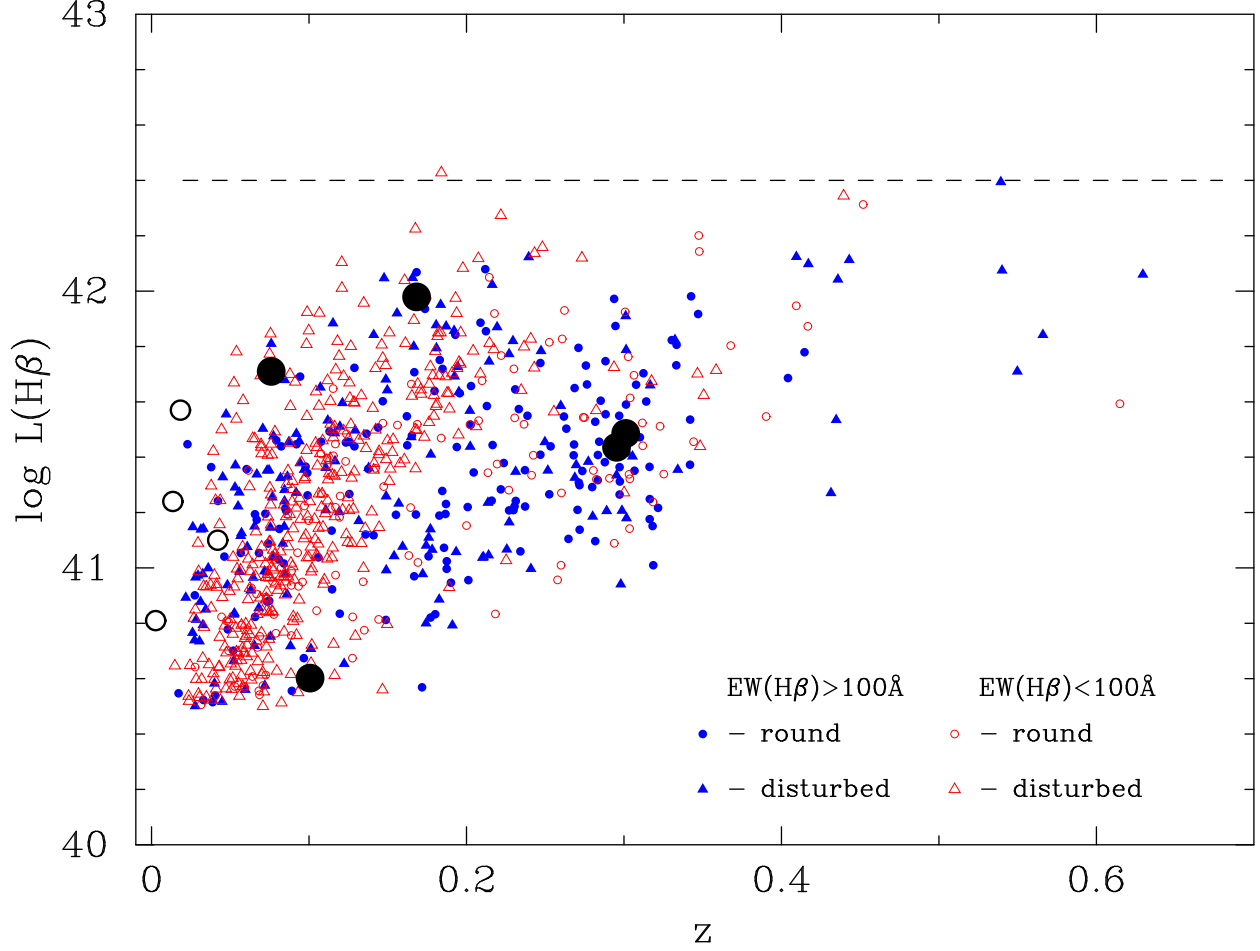


Fig. 2.— Extinction-corrected H β luminosity $L(\text{H}\beta)$ vs. redshift z for the LCG sample. LCGs with $\text{EW}(\text{H}\beta) \geq 100\text{\AA}$ are shown by filled symbols. Those with a round shape and those with some signs of disturbed morphology are shown respectively by small filled circles and small filled triangles. LCGs with $50\text{\AA} \leq \text{EW}(\text{H}\beta) < 100\text{\AA}$ are shown by open symbols. Those with a round shape and those with some signs of disturbed morphology are shown respectively by small open circles and small open triangles. Well-studied local LCGs, also known as Blue Compact Dwarf galaxies, such as Mrk 930, SBS 0335–052E, HS 0837+4717 and II Zw 40 are shown by large open circles. Low-metallicity AGN candidates from Izotov & Thuan (2008) and Izotov et al. (2010) are shown by large filled circles.

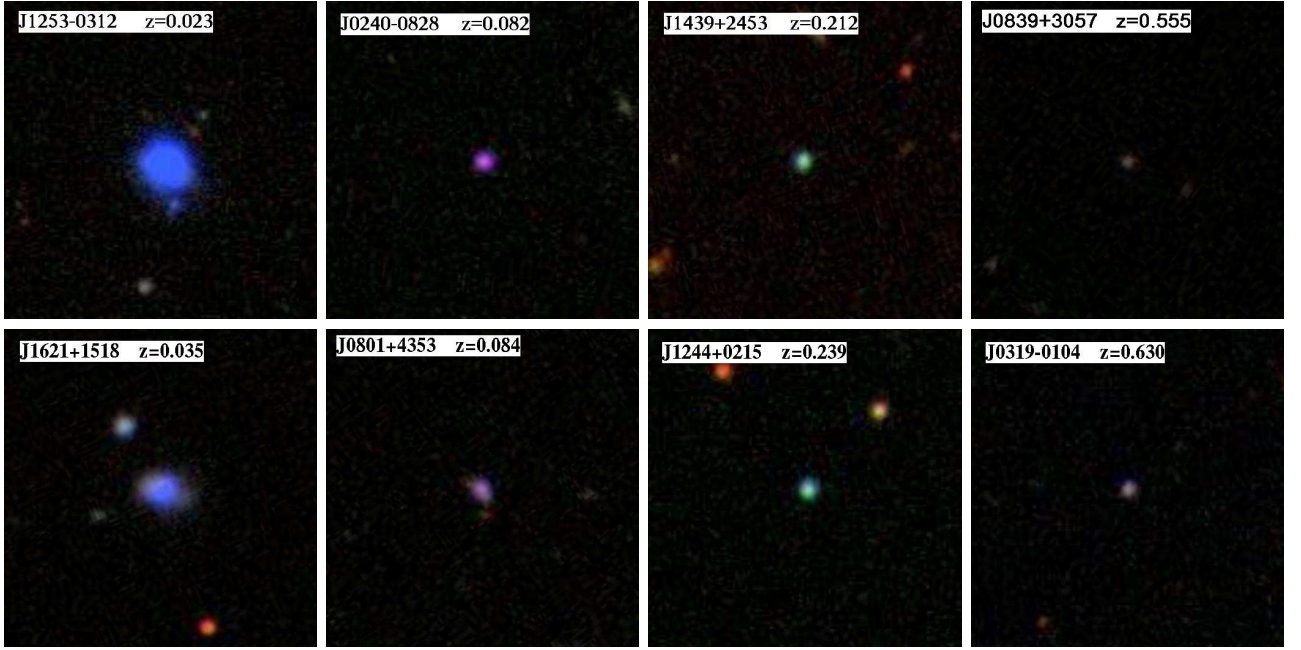


Fig. 3.— $50'' \times 50''$ SDSS images of LCGs in order of increasing redshift from left to right. LCGs from subsample 1 with a round shape are shown in the upper panel, while LCGs from subsample 2 with some evidence of elongated structure and/or disturbed morphology are shown in the lower panel.

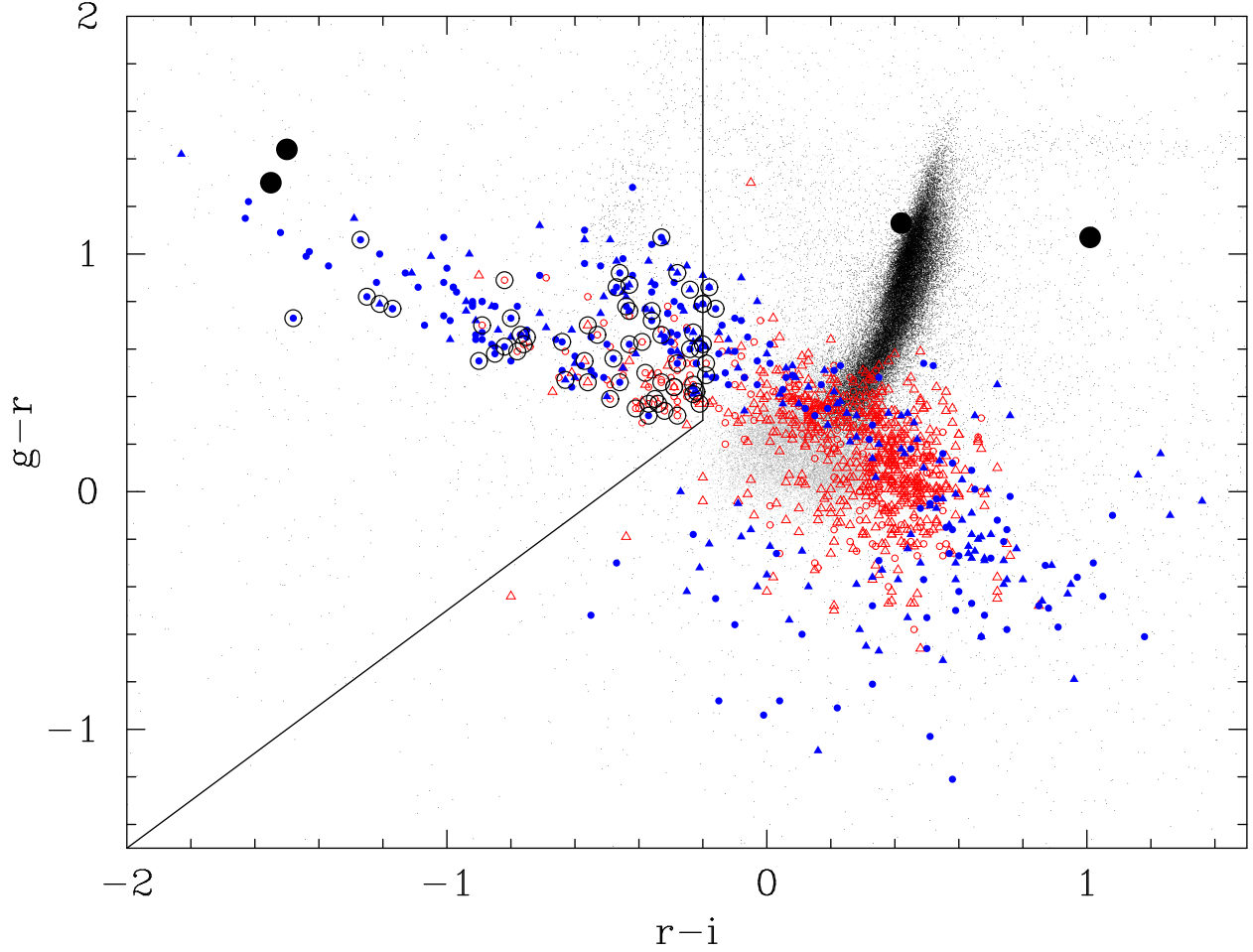


Fig. 4.— $(g - r) - (r - i)$ color-color diagram for LCGs. The symbols for the various types of objects are the same as in Fig. 2. Galaxies common with the green pea sample of Cardamone et al. (2009) are encircled. Low-metallicity AGNs from Izotov & Thuan (2008) are shown by large filled circles. The two solid lines are the dividing lines used by Cardamone et al. (2009) for selection of green pea galaxies. For comparison, a representative sample of SDSS “normal” galaxies (black dots) and QSOs (Schneider et al. 2010) (grey dots) is also shown.

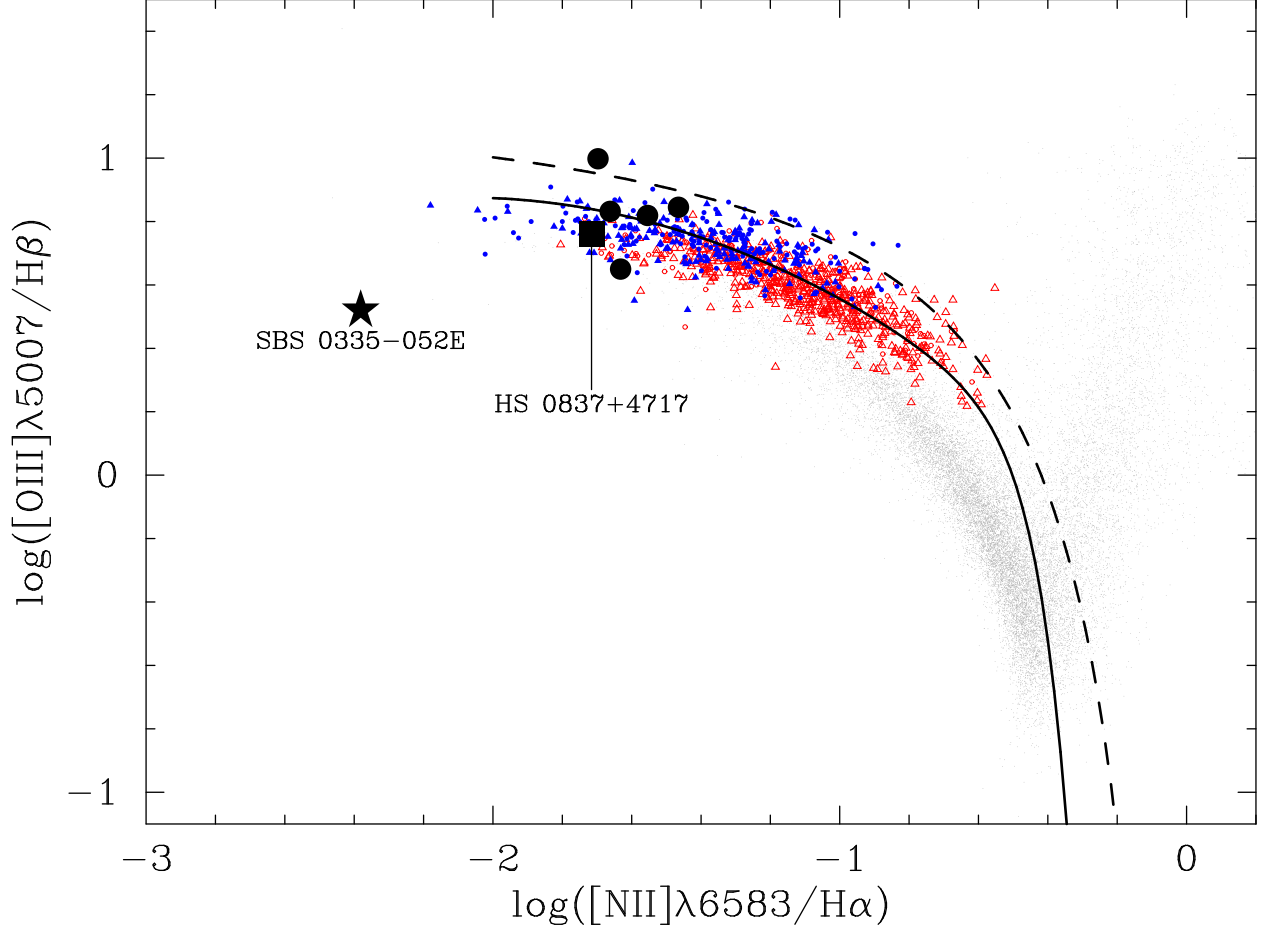


Fig. 5.— The Baldwin-Phillips-Terlevich (BPT) diagram (Baldwin et al. 1981) for narrow emission lines. LCGs are shown by small open and filled symbols, their meaning being the same as in Fig. 2. Also, plotted are the 100 000 emission-line galaxies from SDSS DR7 (cloud of grey dots), the five low-metallicity AGNs from Izotov & Thuan (2008) and Izotov et al. (2010) (filled circles), and the two well-studied BCDs SBS 0335-052E and HS 0837+4717. The dashed line from Kauffmann et al. (2003) and the solid line from Stasińska et al. (2006) separate star-forming galaxies from active galactic nuclei.

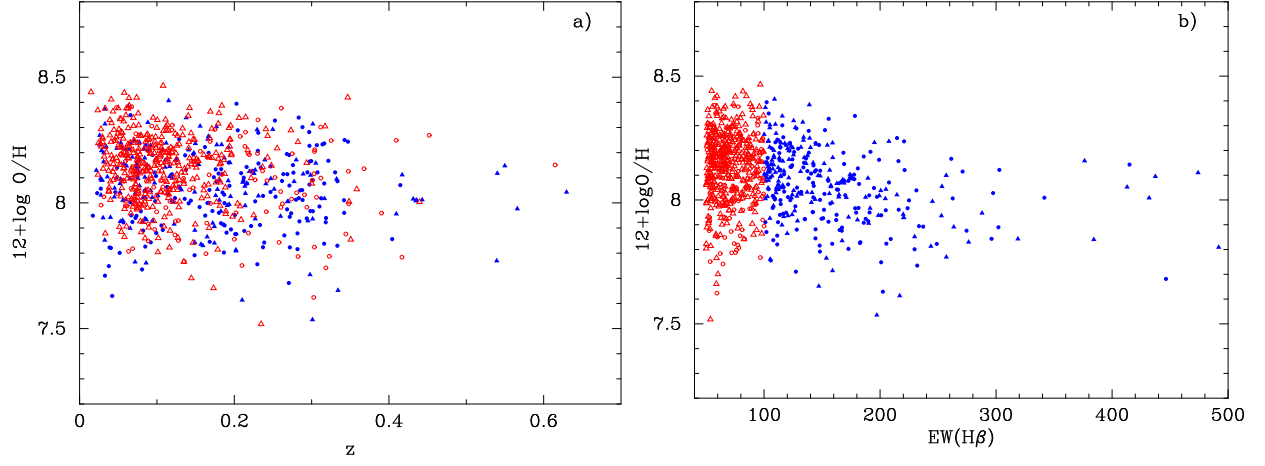


Fig. 6.— Oxygen abundance $12 + \log O/H$ (a) vs. redshift z and (b) vs. the equivalent width $EW(H\beta)$ of the $H\beta$ emission line. The LCGs are shown by symbols with the same meaning as in Fig. 2.

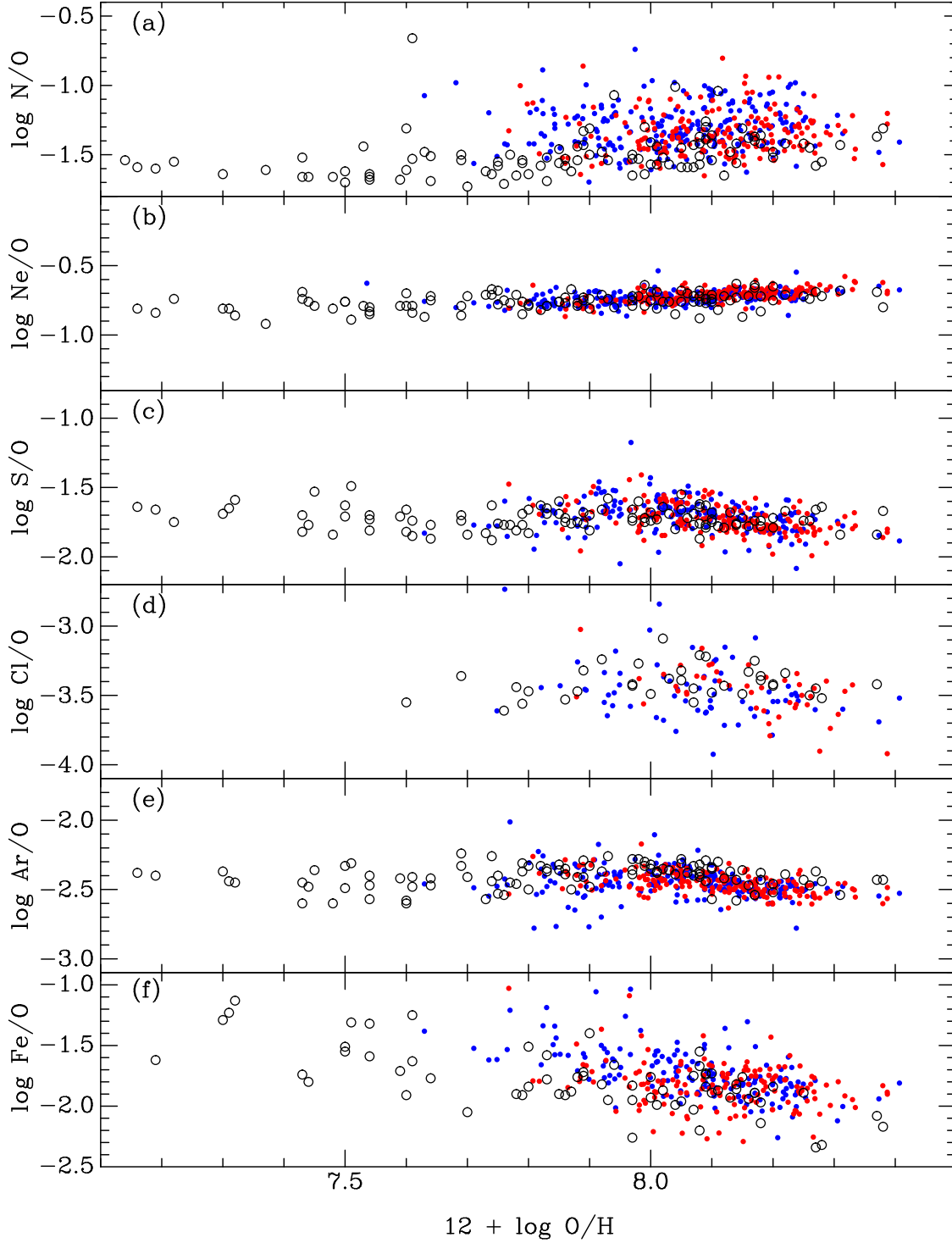


Fig. 7.— Abundance ratios (a) $\log \text{N}/\text{O}$, (b) $\log \text{Ne}/\text{O}$, (c) $\log \text{S}/\text{O}$, (d) $\log \text{Cl}/\text{O}$, (e) $\log \text{Ar}/\text{O}$ and (f) $\log \text{Fe}/\text{O}$ vs. oxygen abundance $12 + \log \text{O}/\text{H}$ for emission-line galaxies. Large open circles denote galaxies from the HeBCD sample (Izotov et al. 1994; Izotov & Thuan 2004), and small filled circles represent LCGs (this paper).

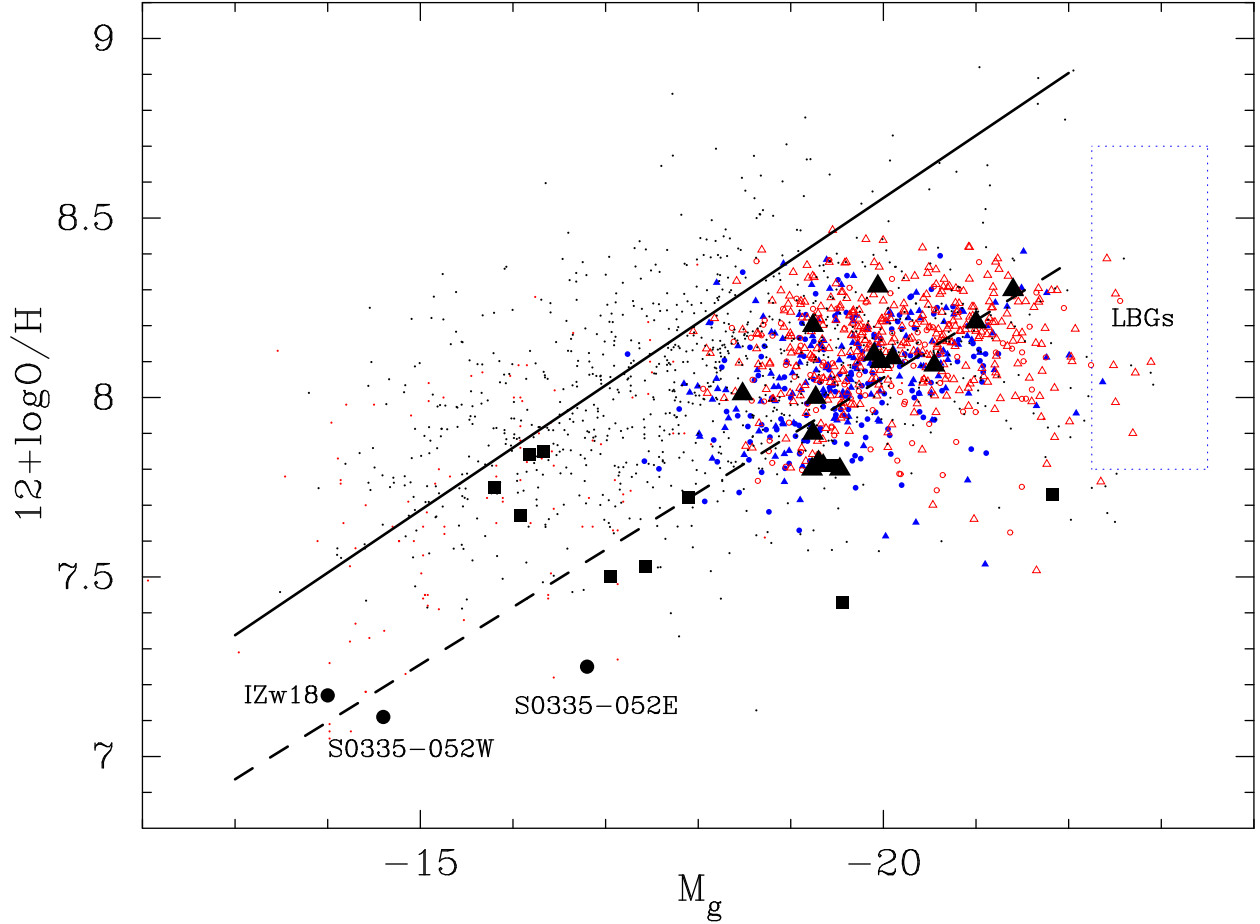


Fig. 8.— Luminosity-metallicity relation for emission-line galaxies. LCGs are shown by the same symbols as in Fig. 2 (filled and open circles and triangles). The emission-line galaxies studied by Guseva et al. (2009) are shown by dots. The luminosity-metallicity relation for these galaxies is fitted by a solid line (Guseva et al. 2009). The most metal-poor local BCDs – I Zw 18, SBS 0335–052W and SBS 0335–052E– are shown by large filled circles (Guseva et al. 2009). The extremely metal-poor emission-line galaxies at intermediate redshifts $z < 1$ studied by Kakazu et al. (2007) and the luminous metal-poor star-forming galaxies at $z \sim 0.7$ studied by Hoyos et al. (2005) are shown by large filled squares and large filled triangles, respectively. The region occupied by Lyman-break galaxies (LBGs) at $z \sim 3$ studied by Pettini et al. (2001) is indicated by a dotted rectangle. The linear best likelihood fit to the strongly star-forming galaxies, excluding LBGs, is shown by a dashed line.

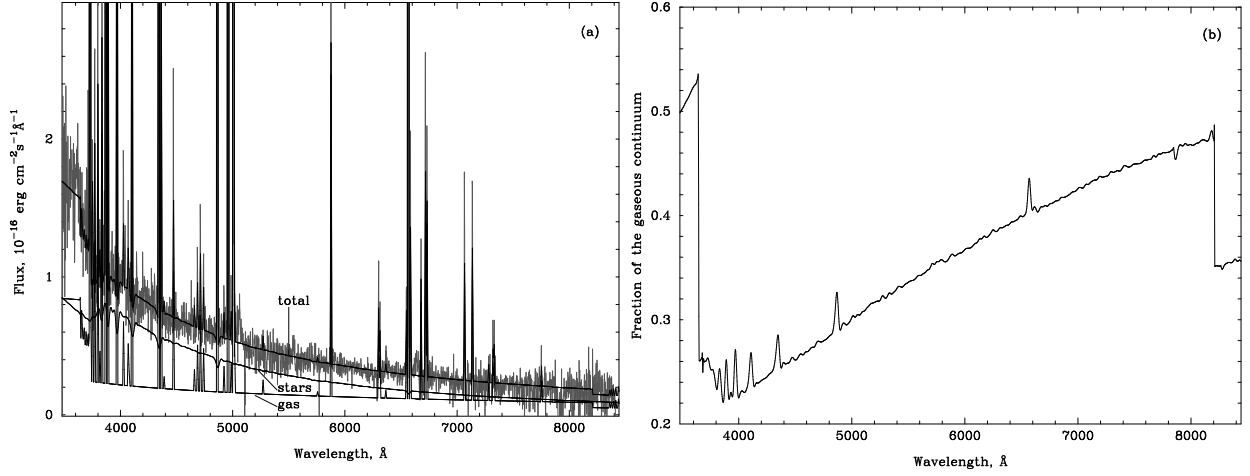


Fig. 9.— (a) Best-fit model SED (solid black line labeled “total”) superposed on the redshift- and extinction-corrected spectrum of the LCG SDSS J0851+5840 (grey line). The separate contributions from the stellar and ionized gas components are shown by black solid lines and labeled “stars” and “gas”, respectively. (b) Gaseous emission fraction vs. wavelength for the modeled spectrum of LCG SDSS J0851+5840 with $\text{EW}(\text{H}\beta) = 303 \text{\AA}$. The two jumps seen at $\sim \lambda 3660 \text{\AA}$ and $\sim \lambda 8200 \text{\AA}$ are due respectively to the hydrogen Balmer and Paschen discontinuities in the ionized gas emission.

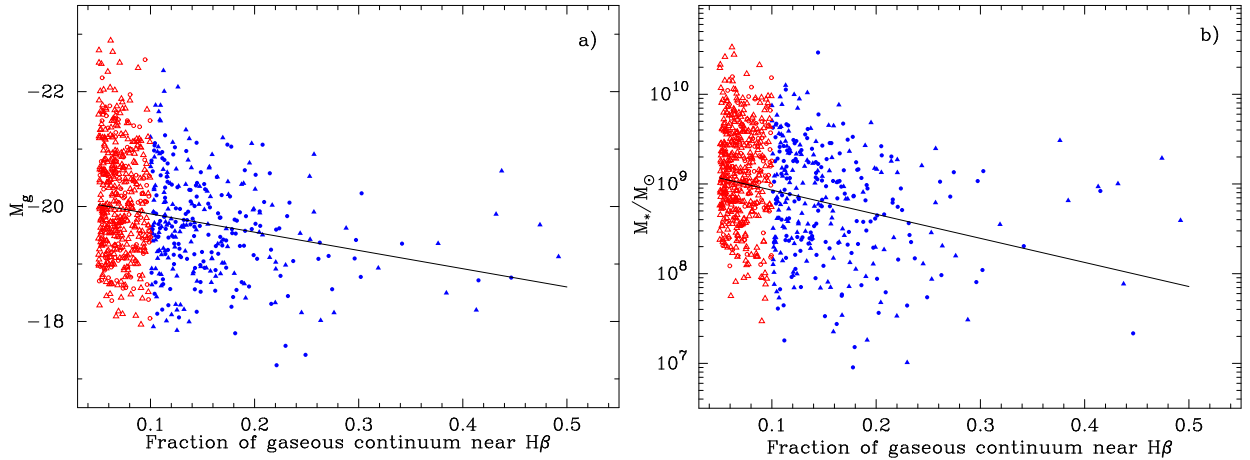


Fig. 10.— (a) The absolute magnitude M_g vs. the fraction of gaseous continuum near the $\text{H}\beta$ emission line. (b) The total stellar mass vs. the fraction of gaseous continuum near the $\text{H}\beta$ emission line. In both panels, the straight line represents the linear best likelihood fit.

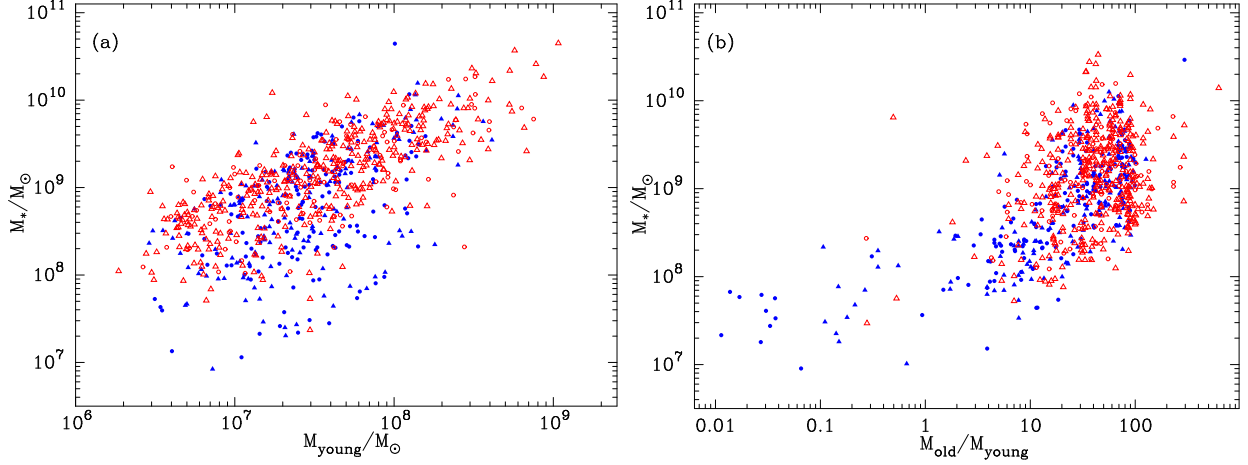


Fig. 11.— (a) The total stellar mass M_* vs. the young stellar population mass $M(\text{young})$. (b) The total stellar mass vs. the young-to-old stellar population mass ratio. The masses of massive galaxies are dominated by an old stellar population, while the masses of low-mass galaxies are dominated by a young stellar population.

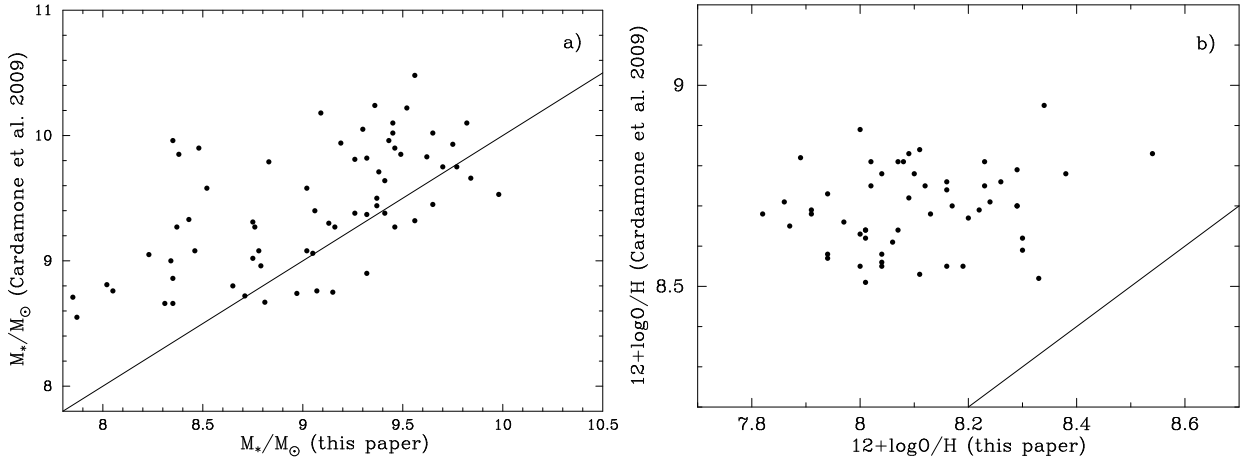


Fig. 12.— Comparison of: (a) stellar masses and (b) oxygen abundances derived for green pea galaxies by Cardamone et al. (2009) and in this paper. Solid lines in both panels are lines of equal values.

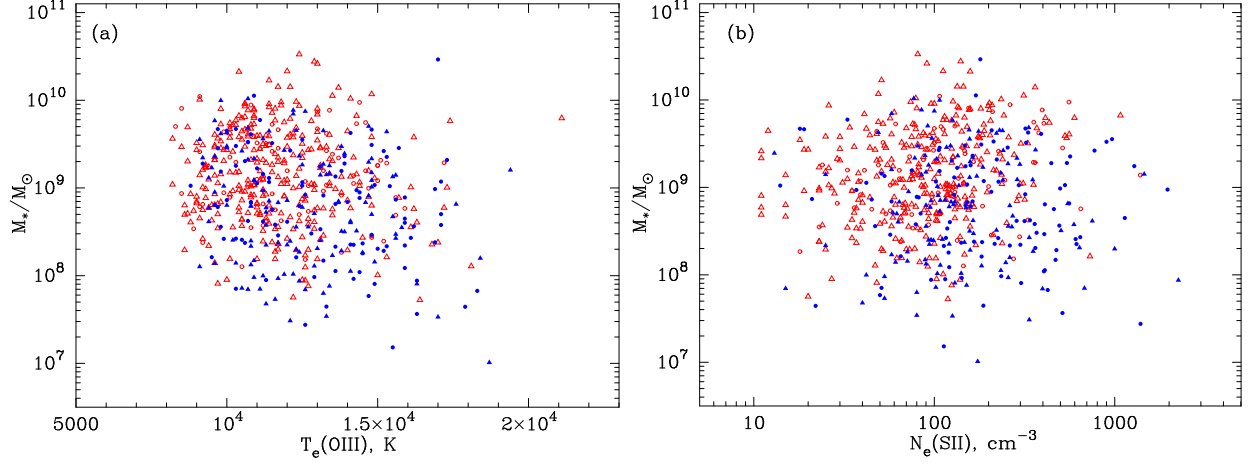


Fig. 13.— The total stellar mass M_* vs. (a) the electron temperature $T_e(\text{O III})$ and (b) the electron number density $N_e(\text{S II})$ of the ionized gas. Both $T_e(\text{O III})$ and $N_e(\text{S II})$ are systematically higher in low-mass galaxies with high $\text{EW}(\text{H}\beta)$.

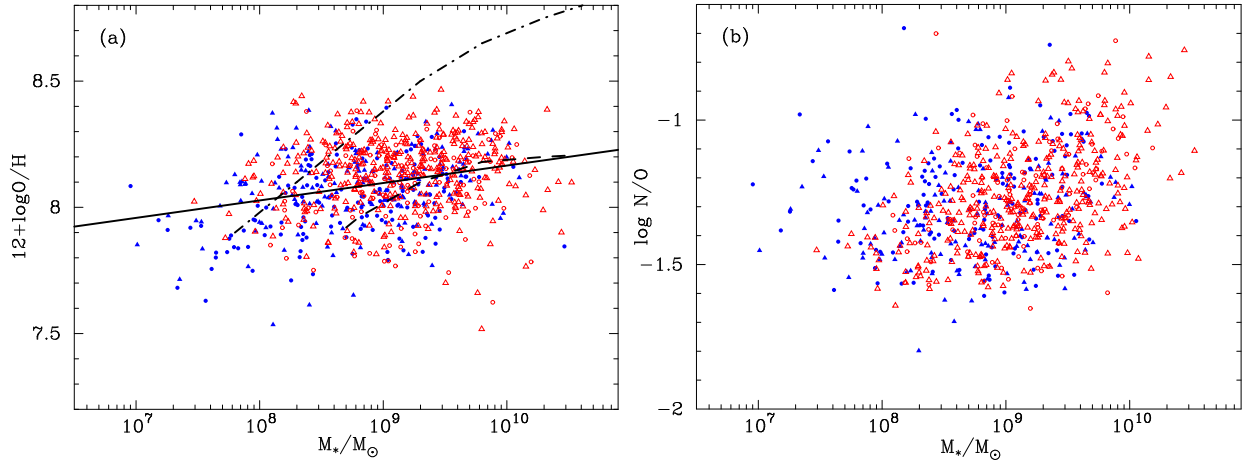


Fig. 14.— (a) Oxygen abundance $12 + \log \text{O}/\text{H}$ vs. stellar mass M_* for the LCG sample. The symbols are the same as in as in Fig. 2. The linear least-squares best fit to the data is shown by the solid line. The fits to the green pea sample and star-forming SDSS galaxies of Amorín et al. (2010) are shown respectively by dashed and dash-dotted lines. (b) The N/O vs. M_* relation for the LCG sample. The symbols are the same as in Fig. 2.

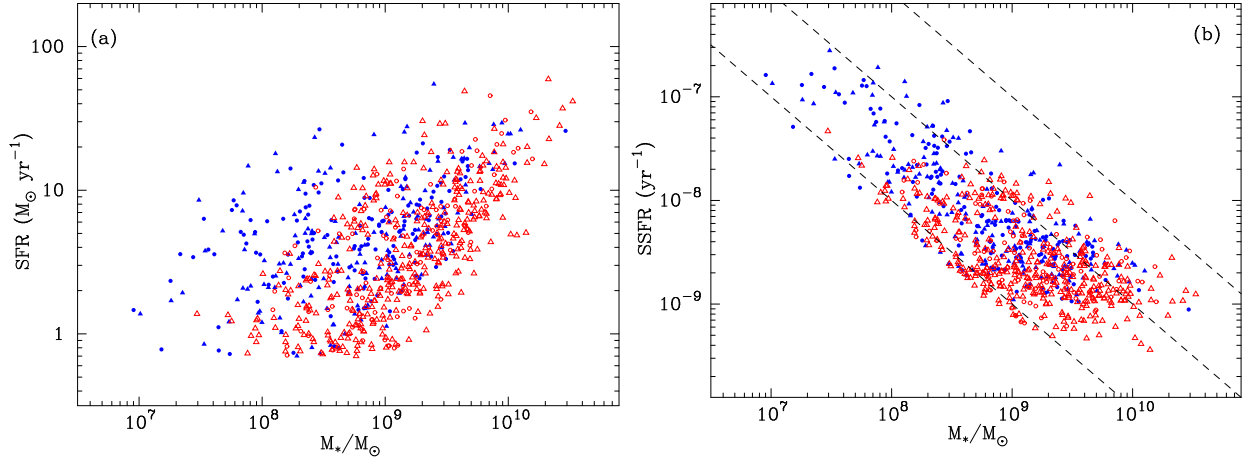


Fig. 15.— (a) The star formation rate $\text{SFR}(\text{H}\alpha)$ and (b) the specific star formation rate $\text{SSFR}(\text{H}\alpha)$ vs. the total stellar mass M_* . The dashed lines in (b) correspond, from left to right, to loci with $\text{SFR} = 1, 10$ and $100 M_\odot \text{ yr}^{-1}$, respectively.

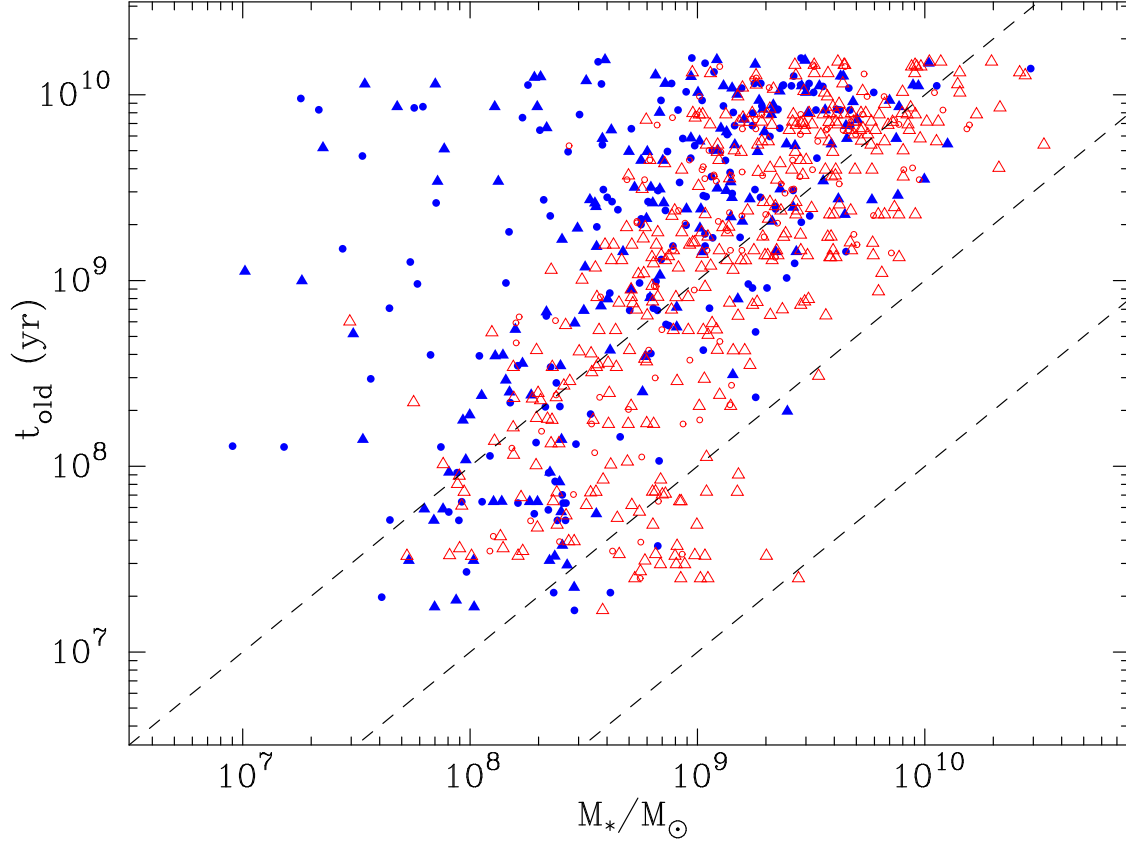


Fig. 16.— Age $t(\text{old})$ of the oldest stellar population in the galaxy vs. its total stellar mass M_* . The dashed lines from left to right correspond to loci with the $\text{SFR} = 1, 10$ and $100 M_\odot \text{ yr}^{-1}$, respectively.